Zentrum für Technomathematik

Fachbereich 3 – Mathematik und Informatik

Using the eXtended finite element method for keyhole-based welding processes

Mischa Jahn Jonathan Montalvo-Urquizo

Report 18–02

Berichte aus der Technomathematik

Report 18–02 **September 2018**

USING THE EXTENDED FINITE ELEMENT METHOD FOR KEYHOLE-BASED WELDING PROCESSES

M. JAHN AND J. MONTALVO-URQUIZO

Abstract. This article addresses the modeling and simulation of keyhole-based welding processes using the eXtended finite element method with multiple indicator function. The welding process is modeled by the heat equation where the keyhole geometry and the interface separating molten and solid area are both represented by level set functions. The keyhole shape is computed by an analytical approach based on the idea of Kaplan and remains constant during the process. In contrast to this, the solid-liquid interface is considered as free boundary whose evolution is described by the two-phase Stefan problem. The coupled problem including two discontinuities is solved using `miXFEM`, an extended finite element method implemented within the `FEniCS` framework. Numerical results are compared to experimental data for different materials.d.

1. Introduction

In modern engineering, processes with time-dependent discontinuities are very common. One example of such processes is welding of metals, where two or more materials are joined. The process consists of the melting and solidification of material around the so-called welding line and there are different welding methods available depending on the application. In this article, we consider keyhole-based welding which is commonly used in the automotive and aeronautic industries, among many others.

In keyhole-based welding, a focused laser beam is used as heat source to generate the melting of material that forms the weld seam after solidification. A characteristic feature of laser based welding is that, for a sufficiently high intensity of the laser beam, a narrow and long vapor channel is formed in the material after a very short unstable period. Furthermore, if the laser beam is translated along the welding line, this vapor channel, called keyhole accompanies its motion, see Figure 1.1. While keyhole-based welding processes are already fit for mass production, there is still need for simulating these process e.g. in order to optimize the weld seam and, hence, the resulting product.

It is well known that inhomogeneous heating cause strong mechanical effects that dominate the welding results in terms of final distortion and residual stresses around the weld seams (cf. e.g. [28, 34]). The shape of the keyhole is responsible for the formation of the liquid melt pool and the inhomogeneous distribution in the temperature field obtained during welding. This is the reason for the high interest on a detailed analysis of its shape and effects.

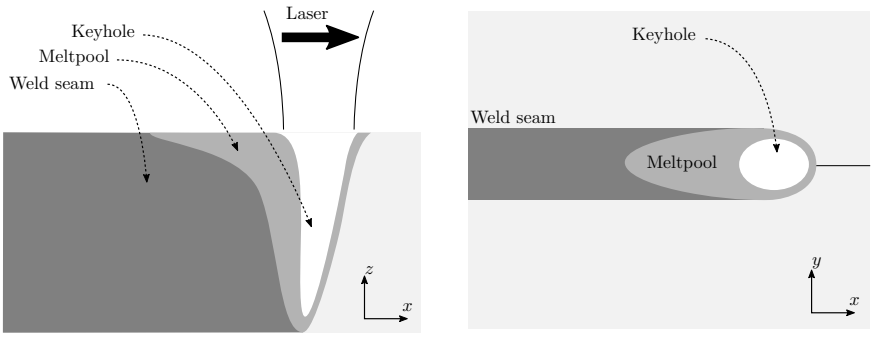

Figure 1.1. Schematic laser welding process, side and top views.

For the simulation of keyhole-based welding processes in this article,the keyhole geometry is computed and used as a boundary condition for the heat equation. Models for computing the keyhole shape exist in many different levels of complexity, going from simple line sources [36] to rather complex models which compute accurate keyhole evolution, as the ones presented in [10]. The probably most common approach to simulate welding processes goes back to [14] and is based on approximating the heat source by a double ellipsoidal geometry. Although the use of this ellipsoidal shapes works well for many welding cases, the welding based on a laser as heat source is mostly determined by the narrow shape of the keyhole, which cannot be approximated using these ellipses.

From a numerical point of view, the modeling and simulation of problems like keyhole welding are very interesting since the keyhole and the solid-liquid phase boundary induce two (arbitrarily) moving physical discontinuities. A flexible method, which has proven to be very suitable for the simulation of such problems, is the extended finite element method (XFEM), see e.g. [12] for an overview. The basic idea of XFEM is to improve a standard finite element method by enriching the discrete function spaces with additional basis functions in order to capture functional discontinuities at the interface location. Thereby, strong discontinuities (jumps) and weak discontinuities (jumps in the derivative) of a function inside an element can be considered. Within the method, a discontinuity is normally represented by the zero level set of a continuous scalar function. By doing so, the physical geometry is decoupled from the computational mesh.

In this article, we use an approach based on XFEM in combination with the level set method to model and simulate the thermal aspects of keyhole-based welding processes for different materials. Neglecting the fluid dynamics of the process, we use an analytical model based on [21] to determine the keyhole shape in subject to material and laser parameters. Once computed, this (fixed) keyhole geometry, represented by the zero level set of a signed distance function, is moved along the material with the welding speed. To include solid-liquid phase transitions, the Stefan problem with sharp interface is considered, which is also represented by the zero level set of a (different) signed distance function. In contrast to the keyhole geometry, the solid-liquid interface is only known at the initial time and its evolution described by the Stefan condition is part of the solution. Based on the level set functions, local Heaviside enrichment is used to enrich the function space for the temperature. As this enrichment generally allows jumps in a function, we use Nitsche's method [31] to introduce internal Dirichlet boundary conditions and enforce continuity. By doing so, we follow a different approach compared to i.a. [2, 9, 24], who successfully applied enriched finite element methods based on weak enrichments to the Stefan problem in level set formulation.

This article is structured as follows: In Section 2, we define the governing equations and boundary conditions for the thermal problem and the level set method which result in a coupled problem. We consider the discretization of the subproblems independently, starting with the thermal problem in Section 3, where we firstly discretize in time to get a series of stationary problems so that we can define a weak formulation for each time step. The subsequent spatial discretization using the extended finite element method is based on Nitsche's approach [31] to include weak internal Dirichlet boundaries [11] at the discontinuities (keyhole wall and the solid-liquid interface). In Section 4, the model for computing the keyhole geometry is presented and a level set function is constructed whose zero level set represents the keyhole shape. In Section 5, the level set problem on a so-called narrow band is considered briefly. This section includes deriving a weak and suitable discrete formulation and comments on a discrete interface representation method as well as techniques to maintain the level set function. After giving some details of the implementation in Section 6, numerical results for keyhole geometries and melt pool shapes for different materials are presented in Section 7. A summary highlighting the most important aspects of the article concludes this paper.

2. Model

Our modeling of a keyhole-based welding process focuses on the thermal aspects and is based on the heat equation. While from a physical point of view, the locations and shapes of both, keyhole and solid-liquid interface, are unknown and part of the solution, we assume that the keyhole shape remains constant during the process and can be computed a priori by a given model. Thus, only the solid-liquid interface given by the Stefan problem describing melting and

solidification is unknown and part of the solution. For the computation of the keyhole geometry, we adapt the approach presented in [21] and use an analytical model of the energy balance at the keyhole wall to approximate the keyhole shape for a quasi-stationary situation, see Section 4. The derived keyhole geometry is then considered as internal (Dirichlet) boundary at which evaporating temperature is assumed and its shape is translated with the laser motion velocity V_{L} along the weld line. Due to this, the model omits (re-)vaporization effects and we assume that no material actually leaves the domain due to vaporization effects and that no plasma or the like arise. Hence, our modular approach consists of

(1) the heat equation with its boundary conditions and the corresponding interface conditions for the keyhole-wall and the solid-liquid interface,
(2) the Stefan problem in level set formulation to describe solid-liquid phase transitions, and
(3) the level set method to represent the (fixed and a priori computed) keyhole geometry and the solid-liquid interface.

`Remark:` Since the only request for the thermal problem is that we have a given keyhole geometry on which a Dirichlet condition for the temperature can be applied, any known keyhole model can be integrated into this approach.

2.1. **Thermal problem.** Let $\Omega \subset \mathbb{R}^3$, with $\partial\Omega$ polygonally, be a fixed domain consisting for $t \in [t_0, t_f]$ of the disjunct regions $\Omega_1(t)$, $\Omega_2(t)$ and $\Omega_3(t)$ that are separated by internal boundaries $\Gamma_1(t)$ (the keyhole wall) and $\Gamma_2(t)$ (the solid-liquid interface), s.t. $\Gamma_1(t) = \overline{\Omega_1(t)} \cap \overline{\Omega_2(t)}$ and $\Gamma_2(t) = \overline{\Omega_2(t)} \cap \overline{\Omega_3(t)}$ and $\Gamma_1(t) \cap \Gamma_2(t) = \emptyset$. We assume that $\Gamma_i(t)$, $i = 1, 2$, is sharp and sufficiently smooth for all $t \in [t_0, t_f]$ and introduce the normal vector $\vec{n}_i(t, \boldsymbol{x})$ to $\Gamma_i(t)$ pointing from Ω_i into Ω_{i+1}.

The temperature field is given by $u\colon \Omega \times [t_0, t_f] \to \mathbb{R}$ with $u|_{\Omega_i} = u_i,\ i \in \{1, 2, 3\}$ and its evolution is described by

$$\rho c \frac{\partial u}{\partial t} - \nabla \cdot (\lambda \nabla u) = f, \quad \text{in } \Omega_1(t) \cup \Omega_2(t) \cup \Omega_3(t),\ t \in (t_0, t_f), \tag{2.1}$$

in which we assume that the density ρ is constant in Ω while the specific heat capacities c_i and the thermal conductivities λ_i are assumed as constant in each subdomain $\Omega_i(t)$ and, therefore, dependent on the time.

For the boundary $\partial\Omega = \Gamma_D \cup \Gamma_N \cup \Gamma_R$ with $\Gamma_D \cap \Gamma_N \cap \Gamma_R = \emptyset$, the following conditions are given

$$u = g_D, \qquad \text{on } \Gamma_D \times (t_0, t_f], \tag{2.2}$$

$$\lambda \frac{\partial u}{\partial \vec{n}} = g_N, \qquad \text{on } \Gamma_N \times (t_0, t_f], \tag{2.3}$$

$$\lambda \frac{\partial u}{\partial \vec{n}} = g_R(u), \qquad \text{on } \Gamma_R \times (t_0, t_f], \tag{2.4}$$

where $\vec{n}$ denotes the outer normal to $\partial\Omega$. Thereby, the function $g_R(u)$ describes the thermal transfer to the environment which we model as combination of Newton's law of cooling and the Stefan-Boltzmann law

$$g_R(u) = g_c(u) + g_r(u) = \alpha(u_a - u) + \epsilon\sigma(u_a^4 - u^4) \tag{2.5}$$

with α being the heat transfer coefficient, u_a denoting the ambient temperature, σ is the Stefan-Boltzmann constant and ϵ is the emissivity of the material. As before, the coefficients α and ϵ are assumed to be constant in each phase and, hence, are time-dependent.

At the keyhole wall $\Gamma_1(t)$ and the solid-liquid phase boundary $\Gamma_2(t)$, we expect the so-called isothermal interface conditions

$$u(\cdot, t) = u_{\Gamma_1} \text{ on } \Gamma_1(t) \quad \text{and} \quad u(\cdot, t) = u_{\Gamma_2} \text{ on } \Gamma_2(t) \tag{2.6}$$

to hold for all times $t \in [t_0, t_f]$ with u_{Γ_1} being the evaporating temperature and u_{Γ_2} being the melting temperature, s.t. $u_{\Gamma_1} > u_{\Gamma_2}$. As a result, it is

$$u(\cdot, t) > u_{\Gamma_1} \qquad \text{in } \Omega_1(t), \tag{2.7}$$

$$u_{\Gamma_1} > u(\cdot, t) > u_{\Gamma_2} \qquad \text{in } \Omega_2(t), \tag{2.8}$$

$$\text{and} \quad u(\cdot, t) < u_{\Gamma_2} \qquad \text{in } \Omega_3(t). \tag{2.9}$$

Initially, the temperature distribution on $\Omega_1(t_0) \cup \Omega_2(t_0) \cup \Omega_3(t_0)$ is given by

$$u(\cdot, t_0) = u_0 \tag{2.10}$$

and

$$\Gamma_1(t_0) = \{\boldsymbol{x} \in \Omega \,:\, u(\boldsymbol{x}, t_0) = u_{\Gamma_1}\} \tag{2.11}$$

$$\Gamma_2(t_0) = \{\boldsymbol{x} \in \Omega \,:\, u(\boldsymbol{x}, t_0) = u_{\Gamma_2}\}. \tag{2.12}$$

2.2. **The level set method.** For the representation of both internal boundaries, the level set method [1, 39] is used. Thus, the location of an arbitrary sharp interface Γ is given by the zero level set of a continuous function $\varphi\colon \Omega \times [t_0, t_f] \to \mathbb{R}$, i.e.

$$\Gamma(t) = \{\boldsymbol{x} \in \Omega \,:\, \varphi(\boldsymbol{x}, t) = 0\}, \quad t \in [t_0, t_f].$$

Given the initial value $\varphi_0(\cdot) = \varphi(\cdot, t_0)$ with zero level set $\Gamma_0 = \Gamma(t_0)$ and boundary conditions on the inflow boundary $\partial\Omega_{\text{in}} := \{\boldsymbol{x} \in \partial\Omega \,:\, \vec{V}(\boldsymbol{x}, t) \cdot \vec{n}(\boldsymbol{x}) < 0,\, t \in [t_0, t_f]\}$ defined by a continuous function $\varphi_{\text{in}}\colon \partial\Omega_{\text{in}} \times [t_0, t_f] \to \mathbb{R}$, the evolution of the level set function φ and consequently of the interface Γ in time can be described by the problem

$$\begin{aligned} \frac{\partial \varphi}{\partial t} + \vec{V} \cdot \nabla \varphi &= 0 && \text{in } \Omega \times [t_0, t_f], \\ \varphi(\cdot, t_0) &= \varphi_0 && \text{in } \Omega, \\ \varphi(\cdot, t) &= \varphi_{\text{in}}(t) && \text{on } \partial\Omega_{\text{in}} \times [t_0, t_f], \end{aligned} \tag{2.13}$$

where $\vec{V} = \vec{V}(\boldsymbol{x}, t)$ is a sufficiently smooth velocity field. While the choice of φ can be (almost) arbitrary, from a numerical point of view it is advantageous to use a so called *signed distance function*, i.e.

$$\varphi(\boldsymbol{x}, t) = \begin{cases} -\min\limits_{\tilde{\boldsymbol{x}} \in \Gamma(t)} \|\boldsymbol{x} - \tilde{\boldsymbol{x}}\|_2, & \text{if } \boldsymbol{x} \in \Omega_1(t) \\ \min\limits_{\tilde{\boldsymbol{x}} \in \Gamma(t)} \|\boldsymbol{x} - \tilde{\boldsymbol{x}}\|_2, & \text{if } \boldsymbol{x} \in \Omega_2(t) \end{cases},$$

which satisfies $\|\nabla \varphi\| = 1$.

Relating to our situation, we introduce two level set functions $\varphi_1,\ \varphi_2 \in C^1(\Omega \times (t_0, t_f)) \cap C^0(\bar{\Omega} \times [t_0, t_f])$ and define Γ_1 as zero level set of φ_1 and Γ_2 as zero level set of φ_2. However, since we assume that the motion of the keyhole geometry is prescribed meaning that $\varphi_1(\boldsymbol{x}, t)$ and $\Gamma_1(t)$ are known for all $t \in [t_0, t_f]$, we only have to solve problem (2.13) for φ_2 which is a priori unknown and part of the solution. For this purpose, we introduce the Stefan condition [37]

$$[\![\lambda \nabla u \cdot \vec{n}_2]\!] = \rho L \vec{V}_{\Gamma_2} \cdot \vec{n}_2 \quad \text{on } \Gamma_2, \tag{2.14}$$

with $[\![\cdot]\!]$ denoting the jump that is defined for a function ϕ by $[\![\phi]\!] = \phi|_{\Omega_1} - \phi|_{\Omega_2}$ and L denoting the material's latent heat. The Stefan condition describes the movement of the interface $\Gamma_2(t)$ in time in terms of its normal velocity $\vec{V}_{\Gamma_2} \cdot \vec{n}_2$ and couples the heat equation with the level set problem.

2.3. **Coupled problem.** Assuming that the level set function $\varphi_1 \in C^1(\Omega \times (t_0, t_f)) \cap C^0(\bar{\Omega} \times [t_0, t_f])$, and hence, the keyhole geometry $\Gamma_1(t)$, is a priori known or can be determined by some approach independently from the thermal problem for $t \in [t_0, t_f]$, our coupled model for a keyhole-based laser welding process reads:
Find the solid-liquid interface $\varphi_2 \in C^1(\Omega \times (t_0, t_f)) \cap C^0(\bar{\Omega} \times [t_0, t_f])$ and the temperature distribution u which is sufficiently smooth, i.e. $u \in \mathcal{C}^0(\bar{\Omega} \times [t_0, t_f])$, $u(\cdot, t)_{|\Omega_i} \in \mathcal{C}^2(\Omega_i(t))$ and

$\partial_t u(\cdot,t) \in C^0(\Omega_1(t) \cup \Omega_2(t) \cup \Omega_3(t))$ for $t \in [t_0, t_f]$ such that

$$
\begin{aligned}
&\rho c \frac{\partial u}{\partial t} - \nabla \cdot (\lambda \nabla u) = f && \text{in } \textstyle\bigcup_{i=1}^{3} \Omega_i(t),\ t \in (t_0, t_f), && \text{(2.15a)}\\
&u = g_D && \text{on } \Gamma_D \times (t_0, t_f], && \text{(2.15b)}\\
&\lambda \frac{\partial u}{\partial \vec{n}} = g_N && \text{on } \Gamma_N \times (t_0, t_f], && \text{(2.15c)}\\
&\lambda \frac{\partial u}{\partial \vec{n}} = g_R(u) && \text{on } \Gamma_R \times (t_0, t_f], && \text{(2.15d)}\\
&u(\cdot, t) = u_{\Gamma_1} && \text{on } \Gamma_1(t), && \text{(2.15e)}\\
&u(\cdot, t) = u_{\Gamma_2} && \text{on } \Gamma_2(t), && \text{(2.15f)}\\
&u(\cdot, t_0) = u_0 && \text{in } \textstyle\bigcup_{i=1}^{3} \Omega_i(t_0), && \text{(2.15g)}
\end{aligned}
$$

$$
[\![\lambda \nabla u \cdot \vec{n}_2]\!] = \rho L \vec{V}_{\Gamma_2} \cdot \vec{n}_2 \qquad \text{on } \Gamma_2(t), \tag{2.16}
$$

$$
\begin{aligned}
&\frac{\partial \varphi_2}{\partial t} + \vec{V}_{\Gamma_2} \cdot \nabla \varphi_2 = 0 && \text{in } \Omega \times [t_0, t_f], && \text{(2.17a)}\\
&\varphi_2(\cdot, t_0) = \varphi_{2,0} && \text{in } \Omega, && \text{(2.17b)}\\
&\varphi_2(\cdot, t) = \varphi_{2,\text{in}}(t) && \text{on } \partial\Omega_{\text{in}} \times [t_0, t_f], && \text{(2.17c)}
\end{aligned}
$$

for given sufficiently smooth data g_D, g_N, g_R u_0, u_{Γ_1}, u_{Γ_2}, $\varphi_{2,0}$, and $\varphi_{2,\text{in}}$.

3. Discretization of the thermal problem

First of all, we introduce the thermal diffusivity $\kappa_i = \frac{\lambda_i}{\rho_i c_i}$, $i = 1, 2, 3$, and scale the equations and boundary conditions accordingly so that there is no coefficient operating on the time derivate. The resulting scaled functions are indicated by the symbol $\bar{\cdot}$. We discretize the thermal problem using Rothe's method that means we approximate the (sufficiently smooth) time derivative by a finite difference approximation and transform the problem into a sequence of quasi-stationary problems. These problems can then be formulated variationally and discretized in space by using the eXtended finite element method in combination with Nitsche's approach [31].

3.1. Discretization in time.

Discretizing the time interval $[t_0, t_f]$ by $N_t + 1$ time steps into $t_n = t_0 + n\Delta t,\ n = 0, \dots, N_t$, where Δt denotes the time step size, we apply the implicit Euler time discretization to the thermal problem which then reads: For $n = 0, \dots, N_t - 1$, find $u^{n+1} \approx u(\cdot, t_{n+1})$ such that

$$
\begin{aligned}
&\frac{u^{n+1}}{\Delta t} - \nabla \cdot \left(\kappa^{n+1} \nabla u^{n+1}\right) = \bar{f}^{n+1} + \frac{u^n}{\Delta t}, && \text{in } \textstyle\bigcup_{i=1}^{3} \Omega_i(t_{n+1}), && \text{(3.1)}\\
&u^{n+1} = g_D^{n+1}, && \text{on } \Gamma_D(t_{n+1}), && \text{(3.2)}\\
&\kappa^{n+1} \frac{\partial u^{n+1}}{\partial \vec{n}} = \bar{g}_N^{n+1}, && \text{on } \Gamma_N(t_{n+1}), && \text{(3.3)}\\
&\kappa^{n+1} \frac{\partial u^{n+1}}{\partial \vec{n}} = \bar{g}_R^{n+1}(u^{n+1}), && \text{on } \Gamma_R(t_{n+1}), && \text{(3.4)}\\
&u^{n+1} = u_{\Gamma_1}, && \text{on } \Gamma_1(t_{n+1}), && \text{(3.5)}\\
&u^{n+1} = u_{\Gamma_2}, && \text{on } \Gamma_2(t_{n+1}). && \text{(3.6)}
\end{aligned}
$$

The non-linear term $u(t)^4$ in $\bar{g}_R(u)$, cf. (2.5), can be linearized in time using the Taylor approximation. It is

$$
\begin{aligned}
u(t_{n+1})^4 &= u(t_n)^4 + \frac{\partial u(t_n)^4}{\partial u(t_n)} \left(u(t_{n+1}) - u(t_n)\right) + \mathcal{O}(u(t_{n+1}) - u(t_n))^2\\
&= u(t_n)^4 + 4u(t_n)^3 \left(u(t_{n+1}) - u(t_n)\right)\\
&= -3u(t_n)^4 + 4u(t_n)^3 u(t_{n+1})
\end{aligned} \tag{3.7}
$$

Using this, $\bar{g}_R(u)$ can be split it into an explicit part

$$\bar{g}_R^{\text{expl}}(u(t_n)) = \bar{\alpha}^{n+1}u(t_n) + \bar{\epsilon}^{n+1}\sigma u_a^4 + 3u(t_n)^4 \tag{3.8}$$

and an implicit part

$$\bar{g}_R^{\text{impl}}(u(t_{n+1})) = -\bar{\alpha}^{n+1}u(t_{n+1}) - 4\bar{\epsilon}^{n+1}\sigma u(t_n)^3 u(t_{n+1}) \tag{3.9}$$

and the latter will be shifted to the left-hand-side of equation (3.4).

For a fixed $n \in \{0, \dots, N_t - 1\}$, we use the notation $\xi = \frac{1}{\Delta t}$ and obviate the time dependency by setting $\Omega_i := \Omega_i(t_{n+1})$, $i = 1, 2, 3$, $u := u^{n+1}$, etcetera. After summarizing the right-hand-side in (3.1) by $\tilde{f}$ and splitting $\bar{g}_R^{n+1}(u^{n+1})$ in an explicit and implicit part, we end up with the stationary problem

$$\xi u - \nabla \cdot (\kappa \nabla u) = \tilde{f}, \qquad \text{in } \bigcup\nolimits_{i=1}^{3} \Omega_i, \tag{3.10}$$

$$u = g_D, \qquad \text{on } \Gamma_D, \tag{3.11}$$

$$\kappa \frac{\partial u}{\partial \vec{n}} = \bar{g}_N, \qquad \text{on } \Gamma_N, \tag{3.12}$$

$$\kappa \frac{\partial u}{\partial \vec{n}} - \bar{g}_R^{\text{impl}}(u) = \bar{g}_R^{\text{expl}}, \qquad \text{on } \Gamma_R, \tag{3.13}$$

$$u = u_{\Gamma_1}, \qquad \text{on } \Gamma_1, \tag{3.14}$$

$$u = u_{\Gamma_2}, \qquad \text{on } \Gamma_2. \tag{3.15}$$

whose solution represents an approximation of the temperature distribution for each time step.

3.2. **Weak formulation.** In order to solve the given problem using the extended finite element method, we introduce the affine space

$$H^1_{g_D}\left(\bigcup\nolimits_{i=1}^{3} \Omega_i\right) := \left\{v \in L_2(\Omega) \,:\, v|_{\Omega_i} \in H^1(\Omega_i),\, i = 1, 2, 3,\, v|_{\Gamma_D} = g_D\right\},$$

where each element $v \in H^1_{g_D}\left(\bigcup_{i=1}^{3} \Omega_i\right)$ can be restricted onto a subdomain Ω_i denoted by $v_i := v|_{\Omega_i}$. While we choose the general setting with g_D as Dirichlet boundary condition (in trace sense), setting $g_D = 0$ leads to the more familiar Hilbert space $H^1_0\left(\bigcup_{i=1}^{3} \Omega_i\right)$ which will be used in (3.19). For functions $u, v \in H^1_{g_D}\left(\bigcup_{i=1}^{3} \Omega_i\right) \subset H^1\left(\bigcup_{i=1}^{3} \Omega_i\right)$, we define

$$(u, v)_{H^1\left(\bigcup_{i=1}^{3} \Omega_i\right)} := (u, v)_{H^1(\Omega_1)} + (u, v)_{H^1(\Omega_2)} + (u, v)_{H^1(\Omega_3)} \tag{3.16}$$

with

$$(u_i, v_i)_{H^1(\Omega_i)} := \int_{\Omega_i} \nabla u_i \nabla v_i d\boldsymbol{x}, \quad i = 1, 2, 3. \tag{3.17}$$

By using this definition and the L^2-norm we end up with the norm

$$\left(\|\cdot\|^2_{L^2(\Omega)} + |\cdot|^2_{H^1\left(\bigcup_{i=1}^{3} \Omega_i\right)}\right)^{1/2} =: \|\cdot\|_{H^1\left(\bigcup_{i=1}^{3} \Omega_i\right)} \tag{3.18}$$

and define the corresponding Hilbert space

$$V_0 := \left\{v \in H^1_0\left(\bigcup\nolimits_{i=1}^{3} \Omega_i\right) \,:\, v|_{\Gamma_j} = 0,\, j = 1, 2\right\} \tag{3.19}$$

and the affine space

$$V_\Gamma := \left\{v \in H^1_{g_D}\left(\bigcup\nolimits_{i=1}^{3} \Omega_i\right) \,:\, v|_{\Gamma_j} = u_{\Gamma_j},\, j = 1, 2\right\} \tag{3.20}$$

where the interface conditions are introduced in a trace sense, as before. A weak formulation of the problem (3.10) is then given by: For $\xi, \kappa \in L^\infty(\Omega)$, $\tilde{f} \in L^2(\Omega)$, $\bar{g}_N \in L^2(\Gamma_N)$ and $\bar{g}_R^{\text{impl}}(u)$, $\bar{g}_R^{\text{expl}} \in L^2(\Gamma_R)$ find $u \in V_\Gamma$ s.t.

$$\begin{aligned}(\xi u, v)_{L_2\left(\bigcup_{i=1}^{3} \Omega_i\right)} + (\kappa u, v)_{H^1\left(\bigcup_{i=1}^{3} \Omega_i\right)} - (\bar{g}_R^{\text{impl}}(u), v)_{L^2(\Gamma_R)} \\ = (\tilde{f}, v)_{L^2(\Omega)} + (\bar{g}_N, v)_{L^2(\Gamma_N)} + (\bar{g}_R^{\text{expl}}, v)_{L^2(\Gamma_R)}\end{aligned} \tag{3.21}$$

for all $v \in V_0$.

3.3. **Discretization in space using Nitsche's method.** Let $\{\mathcal{S}_h\}_{h>0}$ be a family of shape regular triangulations consisting of tetrahedrons and h is the maximum diameter $h = \max_{S\in\mathcal{S}_h} \operatorname{diam}(S)$. Furthermore, let $\Omega_{i,h}$, $i = 1, 2, 3$, be the discrete counterparts of Ω_i separated by (at this point arbitrary) approximations $\Gamma_{j,h}$, $j = 1, 2$, of Γ and $S_i := S \cap \Omega_{i,h}$ the part of S in $\Omega_{i,h}$.

As the interfaces $\Gamma_{j,h}$ are not explicitly considered as facets within the triangulation, the conditions $v|_{\Gamma_{1,h}} = u_{\Gamma_1}$ and $v|_{\Gamma_{2,h}} = u_{\Gamma_2}$ cannot be included into the discrete function space in the same way as the outer Dirichlet condition on Γ_D. Thus, we introduce for $k \in \mathbb{N}$ the function spaces

$$V_{h,g_D}^k := \left\{ v \in H^1_{g_D}\left(\bigcup\nolimits_{i=1}^3 \Omega_{i,h}\right) \,:\, v_i \in C^0(\Omega_{i,h}),\, v|_{S_i} \in \mathbb{P}_k,\, S \in \mathcal{S}_h \right\} \tag{3.22}$$

and

$$V_h^k := \left\{ v \in H^1\left(\bigcup\nolimits_{i=1}^3 \Omega_{i,h}\right) \,:\, v_i \in C^0(\Omega_{i,h}),\, v|_{S_i} \in \mathbb{P}_k,\, S \in \mathcal{S}_h \right\}, \tag{3.23}$$

where the restriction v_i of a function v has to be continuous on $\Omega_{i,h}$, $i = 1, 2, 3$, but not on $\Omega_h = \Omega_{1,h} \cup \Omega_{2,h} \cup \Omega_{3,h}$, and add the interface conditions weakly to the problem using Nitsche's method [31].

Following [11], the discrete formulation of (3.10) is given by: Find $u_h \in V_{h,g_D}^k$ s.t.

$$a(u_h, v_h) + \sum\nolimits_{i=1}^4 a_i(u_h, v_h) = L(v_h) + \sum\nolimits_{i=1}^4 L_i(v_h) \tag{3.24}$$

for all $v_h \in V_{h,0}^k$. The bilinear forms and linear forms are defined as

$$a(u_h, v_h) = \int_{\bigcup_{i=1}^3 \Omega_{i,h}} (\xi u_h v_h d + \kappa \nabla u_h \nabla v_h)\, d\boldsymbol{x} - \int_{\Gamma_{R,h}} \bar{g}_R^{\text{impl}}(u) v_h d\boldsymbol{s} \tag{3.25}$$

$$\begin{aligned} a_1(u_h, v_h) = &- \int_{\Gamma_{1,h}} \kappa_1 \nabla u_{1,h} \cdot \vec{n}_{1,h} v_{1,h} d\boldsymbol{c} - \int_{\Gamma_{1,h}} \kappa_1 \nabla v_{1,h} \cdot \vec{n}_{1,h} u_{1,h} d\boldsymbol{c} \\ &+ \int_{\Gamma_{1,h}} \mu u_{1,h} v_{1,h} d\boldsymbol{c} \end{aligned} \tag{3.26}$$

$$\begin{aligned} a_2(u_h, v_h) = &\int_{\Gamma_{1,h}} \kappa_2 \nabla u_{2,h} \cdot \vec{n}_{1,h} v_{2,h} d\boldsymbol{c} + \int_{\Gamma_{1,h}} \kappa_2 \nabla v_{2,h} \cdot \vec{n}_{1,h} u_{2,h} d\boldsymbol{c} \\ &+ \int_{\Gamma_{1,h}} \mu u_{2,h} v_{2,h} d\boldsymbol{c} \end{aligned} \tag{3.27}$$

$$\begin{aligned} a_3(u_h, v_h) = &- \int_{\Gamma_{2,h}} \kappa_2 \nabla u_{2,h} \cdot \vec{n}_{2,h} v_{2,h} d\boldsymbol{c} - \int_{\Gamma_{2,h}} \kappa_2 \nabla v_{2,h} \cdot \vec{n}_{2,h} u_{2,h} d\boldsymbol{c} \\ &+ \int_{\Gamma_{2,h}} \mu u_{2,h} v_{2,h} d\boldsymbol{c} \end{aligned} \tag{3.28}$$

$$\begin{aligned} a_4(u_h, v_h) = &\int_{\Gamma_{3,h}} \kappa_3 \nabla u_{3,h} \cdot \vec{n}_{2,h} v_{3,h} d\boldsymbol{c} + \int_{\Gamma_{3,h}} \kappa_3 \nabla v_{3,h} \cdot \vec{n}_{2,h} u_{3,h} d\boldsymbol{c} \\ &+ \int_{\Gamma_{3,h}} \mu u_{3,h} v_{3,h} d\boldsymbol{c} \end{aligned} \tag{3.29}$$

$$L(v_h) = \int_{\bigcup_{i=1}^3 \Omega_{i,h}} \tilde{f} v_h d\boldsymbol{x} + \int_{\Gamma_{N,h}} \bar{g}_N v_h d\boldsymbol{s} + \int_{\Gamma_{R,h}} \bar{g}_R^{\text{expl}} v_h d\boldsymbol{s} \tag{3.30}$$

$$L_1(v_h) = - \int_{\Gamma_{1,h}} \kappa_1 \nabla v_{1,h} \cdot \vec{n}_{1,h} u_{\Gamma_1} d\boldsymbol{c} + \int_{\Gamma_{1,h}} \mu u_{\Gamma_1} v_{1,h} d\boldsymbol{c} \tag{3.31}$$

$$L_2(v_h) = \int_{\Gamma_{1,h}} \kappa_2 \nabla v_{2,h} \cdot \vec{n}_{1,h} u_{\Gamma_1} d\boldsymbol{c} + \int_{\Gamma_{1,h}} \mu u_{\Gamma_1} v_{2,h} d\boldsymbol{c} \tag{3.32}$$

$$L_3(v_h) = -\int_{\Gamma_{2,h}} \kappa_2 \nabla v_{2,h} \cdot \vec{n}_{2,h} u_{\Gamma_2} d\boldsymbol{c} + \int_{\Gamma_{2,h}} \mu u_{\Gamma_2} v_{2,h} d\boldsymbol{c}, \tag{3.33}$$

$$L_4(v_h) = \int_{\Gamma_{2,h}} \kappa_3 \nabla v_{3,h} \cdot \vec{n}_{2,h} u_{\Gamma_2} d\boldsymbol{c} + \int_{\Gamma_{2,h}} \mu u_{\Gamma_2} v_{3,h} d\boldsymbol{c} \tag{3.34}$$

where $0 < \mu \in \mathbb{R}$ is a stability parameter which has to be chosen large enough and can be derived analytically for some situations [11]. In contrast to the continuous situation, it is not trivial to show that the sum of all bilinear forms is coercive. In fact, this property depends heavily on the choice of the stability parameter μ. In this paper, we do not investigate this issue further but assume that there is a unique solution of problem (3.24) for a proper choice of μ.

3.4. **XFEM representation of the function space.** Within the extended finite element method a function is represented by a standard and an enriched part. Since the enrichment is usually locally restricted, only a minor subset of elements needs special attention while most of the simplices and degrees of freedom can be considered just as in the standard finite element context. Hence, the computational additional costs are low and the assembled matrices and vectors are still sparse.

Using a Heaviside enrichment, cf. i.a. [12, 27, 30], $u_h \in V_h^k$, is given by

$$u_h = \sum_{i \in \mathcal{N}} u_i v_i + \sum_{i \in \tilde{\mathcal{N}}_1} \hat{u}_{1,i} H_1 v_i + \sum_{i \in \tilde{\mathcal{N}}_2} \hat{u}_{2,i} H_2 v_i \tag{3.35}$$

with basis functions v_i, $i \in \mathcal{N}$, of the to (3.22) associated standard Lagrangian function space $\tilde{V}_h^k = \{v_h \in C(\Omega_h) \,:\, v_h|_S \in \mathcal{P}_k,\ \forall S \in \mathcal{S}_h\}$ and corresponding coefficients u_i. The index sets of enriched basis functions $\tilde{\mathcal{N}}_j$, $j = 1, 2$, are defined by

$$\tilde{\mathcal{N}}_j := \{i \in \mathcal{N} \,:\, \mathrm{meas}_2(\Gamma_{j,h} \cap \mathrm{supp}(v_i)) > 0,\ v_i \in \tilde{V}_h^k\}, \tag{3.36}$$

$\hat{u}_{1,i}$ and $\hat{u}_{2,i}$ are the enriched coefficients, and

$$H_j(\boldsymbol{x}) = \begin{cases} 1, & \text{for } \boldsymbol{x} \in \Omega_{j+1,h} \\ 0, & \text{else} \end{cases}, \quad j = 1, 2, \tag{3.37}$$

are the Heaviside functions. The advantage of using this type of enrichment, is its flexibility as it can be used for problems with strong and weak discontinuities by adding corresponding conditions using Nitsche's technique.

`Remark:` Although using curved intersection segments and the corresponding adaption of the quadrature rules is possible as shown in [8], $k = 1$ is chosen as polynomial degree in this paper. Thus, the interfaces $\Gamma_{j,h}$ are linear approximations of Γ_j and, consequently, the intersecting segments S_i are linear as well.

4. Keyhole model

As mentioned earlier, any known keyhole model can be used in this approach since we (only) assume that the keyhole geometry can be computed a priori based on the material and laser parameters. Here, we adapt the approach of [21] and compute the keyhole geometry using an analytical approach which is based on considering the heat balance at the keyhole wall. For given material and laser parameters, the heat conduction is then approximated by a moving line source [7, 36] and the local inclination angle yielding the keyhole geometry is computed using a point-by-point scheme that compares absorbed power and conduction losses.

4.1. **Laser model.** Firstly, we introduce a Cartesian coordinate system $(\tilde{x}, y, z)$, where $\tilde{x}$ is the welding direction and -z is the laser beam direction, and the corresponding cylindrical coordinate system (r, ϕ, z). After substituting the $\tilde{x}$-coordinate by $x = \tilde{x} - \vec{V}_{\mathrm{L}}(t - t_0)$ for a constant velocity $\vec{V}_{\mathrm{L}}$ in x-direction, we end up with a *quasi-stationary* situation in a coordinate system related to the laser position.

There might be different modes to distribute the intensity profile forming the laser beam and, for this reason, we consider here the two most common ones used in the welding production,

i.e. a constant intensity profile and a Gaussian-like distributed intensity profile. The intensity maximum I_0 is defined by

$$I_0 = \frac{2P_{\mathrm{L}}}{r_{\mathrm{f0}}^2 \pi} \tag{4.1}$$

with P_{L} denoting the laser power and r_{f0} is the laser beam radius in focus height z_0 which depends, among others, on the wave length of the laser beam. Using this, the intensity profile is given as

$$I_{\mathrm{L}}(r,\phi,z) = \begin{cases} I_0 \left(\frac{r_{\mathrm{f0}}}{r_{\mathrm{f}}(z)}\right)^2 \cdot \exp\left(-\frac{2r^2}{r_{\mathrm{f}}(z)^2}\right), & \text{Gaussian-like distribution,} \\ I_0 \left(\frac{r_{\mathrm{f0}}}{r_{\mathrm{f}}(z)}\right)^2, & \text{constant distribution,} \end{cases} \tag{4.2}$$

where $r_{\mathrm{f}}(z)$ is the current laser beam width

$$r_{\mathrm{f}}(z) = r_{\mathrm{f0}} \left(1 + \left(\frac{z - z_0}{z_{\mathrm{Ray}}}\right)^2\right)^{\frac{1}{2}} \tag{4.3}$$

depending on the Rayleigh length z_{Ray}.

4.2. **Heat conduction at the keyhole wall.** To approximate the heat conduction at the keyhole wall, we use an analytic approach based on a moving line source [7, 36], whose power per unit depth P' and location $\boldsymbol{x}^{\mathrm{HS}}(z)$ depend on $z \in \Omega$. Due to the latter, we have a different coordinate system $(\hat{r}_{\boldsymbol{x}^{\mathrm{HS}}(z)}, \hat{\phi}_{\boldsymbol{x}^{\mathrm{HS}}(z)}, z)$ for every $z \in \Omega$ with origin $\boldsymbol{x}^{\mathrm{HS}}(z)$. To simplify the notation in this section, we shortly write $(\hat{r}, \hat{\phi}, z) := (\hat{r}_{\boldsymbol{x}^{\mathrm{HS}}(z)}, \hat{\phi}_{\boldsymbol{x}^{\mathrm{HS}}(z)}, z)$ and keep in mind that all $\hat{\cdot}$ coordinates depend on $\boldsymbol{x}^{\mathrm{HS}}(z)$ and, especially, on z.

Using the moving line heat source model and the introduced notation, the temperature field $u(\hat{\boldsymbol{x}}, t)$ for a *quasi-stationary* situation with $\partial_t u = 0$ in a semi-infinite work-piece is given by

$$u(\hat{r}, \hat{\phi}, z) = u_a + \frac{P'(\hat{r}, \hat{\phi}, z)}{2\pi\lambda} \cdot K_0(\mathrm{Pe}'\hat{r}) \exp\left(-\mathrm{Pe}'\hat{r}\cos(\hat{\phi})\right) \tag{4.4}$$

with $K_0(\hat{\boldsymbol{x}})$ being the modified Bessel function of second kind and zeroth order, and Pe' is the modified Peclet number

$$\mathrm{Pe}' = \frac{\vec{V}_{\mathrm{L}} \rho c}{2\lambda} = \frac{\vec{V}_{\mathrm{L}}}{2\kappa}, \tag{4.5}$$

cf. [7, 21]. Since evaporating temperature u_{Γ_1} has to be reached for all points $(\hat{r}, \hat{\phi}, z)$ at the keyhole wall, we can transform (4.4) to get a formula to compute the value of the heat source $P'(\hat{r}, \hat{\phi}, z)$ which is then given by

$$P'(\hat{r}, \hat{\phi}, z) = (u_{\Gamma_1} - u_a) \cdot 2\pi\lambda \frac{1}{K_0(\mathrm{Pe}'\hat{r})} \exp\left(\mathrm{Pe}'\hat{r}\cos(\hat{\phi})\right). \tag{4.6}$$

In general, thermal conduction can be described by Fourier's law. Assuming that heat propagates isotropic which means that the isothermal surfaces are concentric spheres, we neglect heat flux in z-direction and consider the heat flow only in radial direction, i.e.

$$\dot{q}(\hat{r}, \hat{\phi}, z) = -\lambda \nabla u \approx -\lambda \partial_{\hat{r}} u. \tag{4.7}$$

Substituting u with (4.4) and differentiating leads to

$$\begin{aligned} \dot{q}(\hat{r}, \hat{\phi}, z) &= -\lambda \frac{\partial u}{\partial \hat{r}} \\ &= \frac{P'(\hat{r}, \hat{\phi}, z)}{2\pi \exp\left(\mathrm{Pe}'\hat{r}\cos\hat{\phi}\right)} \mathrm{Pe}' \left[K_0(\mathrm{Pe}'\hat{r})\cos\hat{\phi} + K_1'(\mathrm{Pe}'\hat{r})\right], \end{aligned} \tag{4.8}$$

with $K_1(\hat{\boldsymbol{x}})$ as modified Bessel function of second kind and first order. With (4.6) as value for $P'(\hat{r}, \hat{\phi}, z)$ to reach evaporating temperature at the keyhole wall, the heat flow at the keyhole wall is

$$q_v(\hat{r}, \hat{\phi}, z) = (u_{\Gamma_1} - u_a)\lambda \mathrm{Pe}' \left(\cos\hat{\phi} + \frac{K_1(\mathrm{Pe}'\hat{r})}{K_0(\mathrm{Pe}'\hat{r})}\right). \tag{4.9}$$

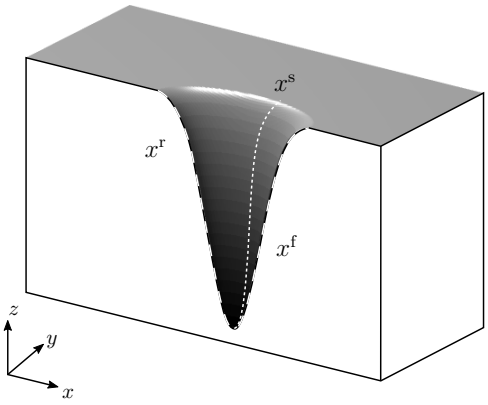

FIGURE 4.1. Keyhole half-geometry with the lines defining its front-back form (long dashes) and its side form (short dashes).

`Remark:` To further simplify the notation, we introduce the transformation function $\psi(\boldsymbol{x}) := \psi(\boldsymbol{x}; \boldsymbol{x}^{\mathrm{HS}}(z)) = \psi(r, \phi, z; \boldsymbol{x}^{\mathrm{HS}}(z))$ which converts coordinates (r, ϕ, z) in the standard coordinate system to coordinates $(\hat{r}, \hat{\phi}, z)$ in the heat source's coordinate system with origin in $\boldsymbol{x}^{\mathrm{HS}}(z)$, $z \in \Omega$.

4.3. **Location of the heat source.** As pointed out before, equation (4.9) is derived assuming that for every $z \in \Omega$ there is a moving line source with energy P' by which evaporating temperature can be obtained at the keyhole wall in this z-layer. It is important to note that the location of the heat source $\boldsymbol{x}^{\mathrm{HS}}(z)$ depend on $z \in \Omega$ and, especially, does not align with the (fixed) laser position.

Given the coordinates $\boldsymbol{x}_i^{\mathrm{f}} = (x_i^{\mathrm{f}}, 0, z_i) = (r_i^{\mathrm{f}}, \phi_i^{\mathrm{f}}, z_i)$ and $\boldsymbol{x}_i^{\mathrm{r}} = (x_i^{\mathrm{r}}, 0, z_i) = (r_i^{\mathrm{r}}, \phi_i^{\mathrm{r}}, z_i)$ in the laser coordinate system, we can approximate the position $\boldsymbol{x}_i^{\mathrm{HS}}$ using an explicit scheme that is based on the distance between front and rear keyhole wall at layer z_i. These coordinates correspond to the lines depicted in the front, back and side of the keyhole geometry from Figure 4.1. More precisely, we have to compute $\boldsymbol{x}_i^{\mathrm{HS}} = (x_i^{\mathrm{HS}}, 0, z_i) = (r_i^{\mathrm{HS}}, \phi_i^{\mathrm{HS}}, z_i)$ s.t. the following equation holds:

$$0 = u_{\Gamma_1} - u_{\Gamma_1} = u(\hat{\boldsymbol{x}}_i^{\mathrm{f}}) - u(\hat{\boldsymbol{x}}_i^{\mathrm{r}}) = u(\boldsymbol{x}_i^{\mathrm{f}} - \boldsymbol{x}_i^{\mathrm{HS}}) - u(\boldsymbol{x}_i^{\mathrm{r}} - \boldsymbol{x}_i^{\mathrm{HS}}) \tag{4.10}$$

which, with (4.4), can be simplified to

$$\begin{aligned} 0 = {} & K_0(\mathrm{Pe}'(r_i^{\mathrm{f}} - r_{i+1}^{\mathrm{HS}}) \exp(-\mathrm{Pe}'(r_i^{\mathrm{f}} - r_i^{\mathrm{HS}})) \\ & - K_0(\mathrm{Pe}'(r_i^{\mathrm{r}} - r_i^{\mathrm{HS}})) \exp(\mathrm{Pe}'(r_i^{\mathrm{r}} - r_i^{\mathrm{HS}})). \end{aligned} \tag{4.11}$$

The function in equation (4.11) has a singularity only at the origin and can be solved to find r_{i+1}^{HS}. This can be numerically well approximated by a bisection method and, once the heat source's location is found, we can define the transformation function $\psi(\boldsymbol{x})$ and evaluate (4.9) not in (r, ϕ, z) but in $(\hat{r}, \hat{\phi}, z)$ for the next z-layer.

4.4. **Computation scheme for the keyhole geometry.** For computing the keyhole geometry, the local heat losses at the keyhole wall are compared to the locally absorbed intensity yielding the relation

$$\tan(\theta(r, \phi, z)) = \frac{q_v(\psi(r, \phi, z))}{\alpha_{\mathrm{fr}} I(r, \phi, z)} = \frac{q_v(\psi(r, \phi, z))}{I_a(r, \phi, z)} = \frac{q_v(\hat{r}, \hat{\phi}, z))}{I_a(r, \phi, z)} \tag{4.12}$$

for the local inclination angle θ, with α_{fr} denoting the Fresnel absorption. Please note that thereby we neglect the dependency of the absorption rate on the angle of incidence but use a constant (mean) Fresnel absorption coefficient.

While (4.12) is an implicit equation and, in principle, allows for a point-wise computation of the entire keyhole geometry, we only use it to determine the front, rear and side wall. Moreover, we consider the equation explicitly by approximating the values on the right-hand-side using

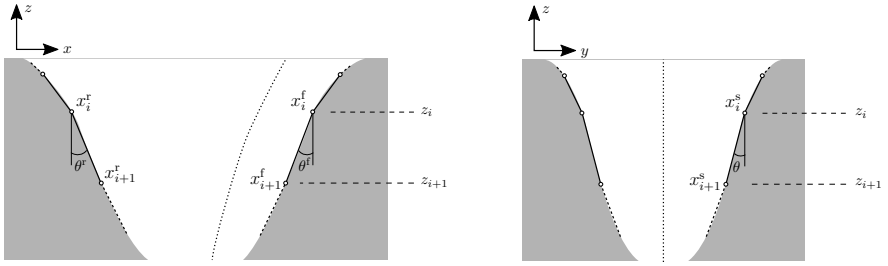

FIGURE 4.2. Discrete iteration to compute the Keyhole shape. *Left:* Side view for computing the front and rear keyhole wall. *Right:* Front view for computing the side view.

the preciously computed value of θ. With this, the explicit point-by-point scheme illustrated in Figure 4.2 is as follows:

(1) Given the keyhole wall points $\boldsymbol{x}_i^{\mathrm{f}}$, $\boldsymbol{x}_i^{\mathrm{r}}$ and $\boldsymbol{x}_i^{\mathrm{s}}$ at the keyhole front, rear and side wall, we firstly compute the location of the heat source $\boldsymbol{x}_i^{\mathrm{HS}}$ by solving (4.10).

(2) With this, we evaluate $q_v(\psi(\boldsymbol{x}_i))$ and $I(\boldsymbol{x}_i)$ to compute $\theta(\boldsymbol{x}_i)$ via relation (4.12) and determine the next keyhole wall points at the front and rear, $\boldsymbol{x}_{i+1}^{\mathrm{f}}$, $\boldsymbol{x}_{i+1}^{\mathrm{r}}$ (in the x-z-plane of the laser's coordinate system) by

$$\begin{aligned} r_{i+1} &= r_i - \Delta z \tan(\theta(\boldsymbol{x}_i)), \\ \phi_{i+1} &= \phi_i = \begin{cases} 0, & \text{at front wall,} \\ \pi, & \text{at rear wall,} \end{cases} \\ z_{i+1} &= z_i - \Delta z, \end{aligned} \tag{4.13}$$

respectively

$$\begin{aligned} x_{i+1} &= x_i - \Delta z \tan(\theta(\boldsymbol{x}_i)), \\ y_{i+1} &= y_i = 0, \\ z_{i+1} &= z_i - \Delta z. \end{aligned} \tag{4.14}$$

(3) Finally, the next point at the keyhole side wall, which is symmetrical to the x-z-plane, is computed by

$$\begin{aligned} x_{i+1} &= x_i^{\mathrm{HS}}, \\ y_{i+1} &= y_i - \Delta z \tan(\theta(\boldsymbol{x}_i)), \\ z_{i+1} &= z_i - \Delta z. \end{aligned} \tag{4.15}$$

Thereby, it is important to note that the x-coordinate of the side wall always aligns with the x-coordinate of the heat source.

The full keyhole geometry is then approximated by defining ellipses for every z_i, using the front and rear wall points as semi-major axes and the side wall points as semi-minor axes in a secondary step. We will elaborate this approach further in Section 4.6.

4.5. **Multiple reflections.** The existence of multi reflections is an essential phenomenon of the laser welding process, as it is responsible for a large amount of energy absorbed into the material pieces. For metallic components, it is known that these reflections can take an absorption factor of around 30% and increase it to values around 80% of the total laser beam energy.

In our formulations, we denoted the intensity in (4.12) by I rather than I_{L} because we have to consider that only a portion of the incident laser beam's intensity I_{L} gets directly absorbed into the material. The remaining intensity $(1-\alpha_{\mathrm{fr}})I_{\mathrm{L}}$ is reflected and (partly) absorbed multiple times within the keyhole causing an overall absorption of up to 80%.

Our computation of the keyhole geometry uses the front, rear and side keyhole walls by a (downwards orientated) point-by-point scheme. Due to this descending computation scheme, we only consider the influence of multi reflections in the negative z-direction, meaning that the impact of a reflection on a previously computed point at the keyhole wall is neglected. Therefore,

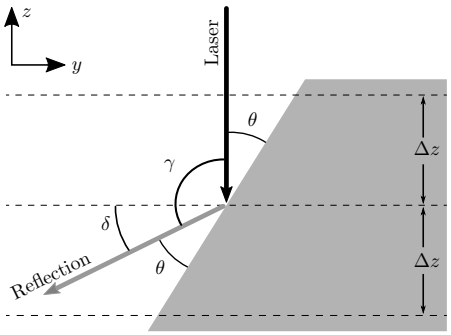

FIGURE 4.3. Scheme for computing the reflection angle for reflected rays.

we can assume that there is no incoming reflection that has to be considered in the computation method for the first $m > 0$ points.

Our approach to consider multi reflections within the computation method for a given point $\boldsymbol{x}_i = (r_i, \phi_i, z_i)$, with $\phi_i \in \{0, \frac{\pi}{2}, \pi\}$ at a keyhole wall with $i \leq m$ consists on performing the following steps:

(1) Compute the inclination angle $\theta(\boldsymbol{x}_{i+1}) = \theta(r_i, \phi_i, z_i)$ by taking (only) $I_{\mathrm{L}}(r_i, \phi_i, z_i)$ into account and then define $\boldsymbol{x}_{i+1}$ according to the scheme presented in Section 4.4.
(2) Determine the reflected intensity $I_r(\boldsymbol{x}_i) = (1 - \alpha_{\mathrm{fr}}) I_{\mathrm{L}}(\boldsymbol{x}_i)$ as well as the reflection angle $\delta(\boldsymbol{x}_i) = \frac{\pi}{2} - 2\theta(\boldsymbol{x}_i)$ relative to the horizontal axis, cf. Figure 4.3.
(3) Introduce a linear function $f_i(r, z) = z_i - \tan(\delta_i)(r + r_i)$ to compute the point of impact of the reflected intensity at the keyhole wall.

For a point $\boldsymbol{x}_j$ with $j > m$ the previously described method is adapted to consider multi reflections starting by the following steps:

(i) Compute a tentative inclination angle $\tilde{\theta}(\boldsymbol{x}_{j+1}) = \tilde{\theta}(r_j, \phi_j, z_j)$ by taking (only) $I_{\mathrm{L}}(r_j, \phi_j, z_j)$ into account and then define a tentative point $\tilde{\boldsymbol{x}}_{j+1}$.
(ii) Evaluate all functions f_i, $i = 0, \ldots, j-1$, at $(\tilde{r}_j, z_j)$ to find the closest points of impact (r_{i_0}, z_{i_0}) and (r_{i_1}, z_{i_1}) forming an interval which contains $(\tilde{r}_j, z_j)$.
(iii) Compute the reflected intensity $I_r(\tilde{r}_j, z_j)$ (acting in $-z$-direction) by interpolating the "cosinus parts" of the corresponding intensities I_{i_0} and I_{i_1}
(iv) Define the total intensity at $(\tilde{r}_j, z_j)$ by $I(r_j, \phi_j, z_j) = I_{\mathrm{L}}(r_j, \phi_j, z_j) + I_r(\tilde{r}_j, \phi_j, z_j)$ and continue with step (1) of the previous scheme using this intensity.

Note that the functions f_i are independent of the angle ϕ_i since a reflection occurs always in normal direction. In our case that means that if an intensity is reflected at the front keyhole wall, it has only an impact of at the rear keyhole wall and vice versa. This is also true for the keyhole side walls. As we only consider these four points, we can model multi reflections without implementing a numerically expensive ray tracing algorithm.

4.6. **Level set representation of the keyhole geometry.** The discrete points at the front, rear and side keyhole wall computed by (4.12) can be used to construct a level set function whose zero level set represents the whole keyhole geometry. Let $\boldsymbol{x}_i^{\mathrm{f}} = (x_i^{\mathrm{f}}, 0, z_i)$, $\boldsymbol{x}_i^{\mathrm{r}} = (x_i^{\mathrm{r}}, 0, z_i)$ and $\boldsymbol{x}_i^{\mathrm{s}_1} = (x_i^{\mathrm{s}}, y_i^{\mathrm{s}}, z_i) = (x_i^{\mathrm{HS}}, y_i^{\mathrm{s}}, z_i)$ resp. $\boldsymbol{x}_i^{\mathrm{s}_2} = (x_i^{\mathrm{s}}, -y_i^{\mathrm{s}}, z_i) = (x_i^{\mathrm{HS}}, -y_i^{\mathrm{s}}, z_i)$, $i = 1, \ldots, M$, be the coordinates of the points at the front, rear and side keyhole wall. For every depth layer z_i, we approximate the keyhole shape by two half-ellipses using the front and rear keyhole wall points as semi-major axes and the side keyhole wall points as semi-minor axes, see Figure 4.4.

By doing this, the half-ellipse connecting $\boldsymbol{x}_i^{\mathrm{f}}$, $\boldsymbol{x}_i^{\mathrm{s}_1}$ and $\boldsymbol{x}_i^{\mathrm{s}_2}$ is given by

$$y^2 = (y_i^{\mathrm{s}})^2 - \frac{(y_i^{\mathrm{s}})^2}{(x_i^{\mathrm{f}})^2}(x - x_i^{\mathrm{s}})^2. \tag{4.16}$$

and the half-ellipse connecting $\boldsymbol{x}_i^{\mathrm{r}}$, $\boldsymbol{x}_i^{\mathrm{s}_1}$ and $\boldsymbol{x}_i^{\mathrm{s}_2}$ is given by

$$y^2 = (y_i^{\mathrm{s}})^2 - \frac{(y_i^{\mathrm{s}})^2}{(x_i^{\mathrm{r}})^2}(x - x_i^{\mathrm{s}})^2. \tag{4.17}$$

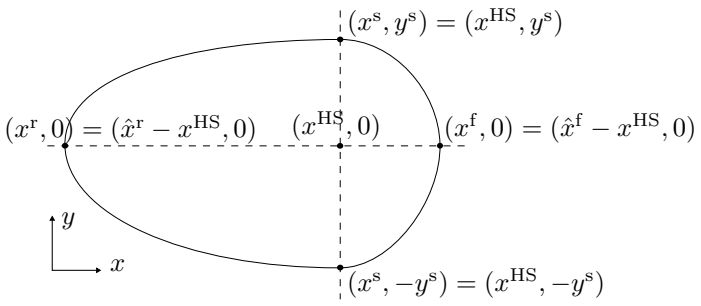

FIGURE 4.4. Keyhole wall approximated at a fixed depth and with a heat source location $(x^{\mathrm{HS}}, 0)$ in both coordinate systems.

Based on this equations, we introduce the level set functions

$$\begin{aligned} \varphi_{1|_{z_i}}(\boldsymbol{x}) &= \varphi(x, y, z_i) \\ &= \begin{cases} \sqrt{(y^2 - (y_i^{\mathrm{s}})^2 - \frac{(y_i^{\mathrm{s}})^2}{(x_i^{\mathrm{f}})^2}(x - x_i^{\mathrm{s}})^2)}, & \text{for } x \geq x^{\mathrm{HS}} \\ \sqrt{(y^2 - (y_i^{\mathrm{s}})^2 - \frac{(y_i^{\mathrm{s}})^2}{(x_i^{\mathrm{r}})^2}(x - x_i^{\mathrm{s}})^2)}, & \text{for } x < x^{\mathrm{HS}} \end{cases} \end{aligned} \tag{4.18}$$

which are signed distance functions whose zero level sets $\Gamma_{1|_{z_i}}$ represents the (2D) keyhole wall for each depth layer z_i, $i = 1, \ldots, M$ in the x-y plane. In the vertical direction, the different ellipses (or equivalently the level set functions) are linearly interpolated between the z-layers to obtain a continuous function φ_1 whose zero level set Γ_1 defines the 3D keyhole geometry. Thereby, φ_1 has to be extended for $z < z_M$ in an arbitrarily but continuous way. For problem (2.15), the keyhole geometry is considered as constant and moves along the welding line at the given welding speed V_{L}. Hence, our sharp interface between keyhole and molten area is given by

$$\Gamma_1(t) = \{\boldsymbol{x} \in \Omega \,|\, \left(\boldsymbol{x} - (t - t_0)\vec{V}_{\mathrm{L}}\right) \in \Gamma_1(t_0),\ t \in [t_0, t_f]\}. \tag{4.19}$$

`Remark:` While in a first step, the discrete keyhole Γ_h is computed using a very small step size Δz for a high precision approximation of the keyhole shape and depth, the level set function φ_1 and the corresponding zero level set Γ_1 are constructed using only a subset of keyhole wall coordinates which contains only about 10% of the previously computed points including the first and the last one. This does not represent any remarkable reduction in precision, as the interfaces are in the end linearly interpolated during the XFEM enrichment of elements.

5. Discretization of the level set problem

In contrast to the keyhole wall Γ_1, whose shape and motion is a priori given by the keyhole model and the process and material parameters for the entire process, the movement of the solid-liquid interface Γ_2 unknown and part of the solution. We use the level set method as representation technique so that the evolution of Γ_2 can be described by the level set problem (2.17). As this is identical with our approach for tackling the two-phase Stefan problem [18], we refer to this paper and only cite the most important aspects here.

We introduce a weak formulation of (2.17) which discretized using the method of lines, i.e. we firstly discretize the problem in space and then in time. Since the level set function may degenerate, we present maintaining methods to preserve the signed distance property and the volume. For efficiency, the level set problem is not considered on the whole domain Ω_h but on a so-called narrow band around the interface $\Gamma_{2,h}$. Therefore, we adapt the formulation and consider the modified transport equation

$$\frac{\partial \varphi_2}{\partial t} + \zeta(\varphi_2)\vec{V}_{\Gamma_2} \cdot \nabla \varphi_2 = 0 \quad \text{in } \Omega \times [t_0, t_f], \tag{5.1}$$

instead, where $\zeta(\varphi_2)$ is some cut-off function specified later. This reformulation is necessary since the solution of the original transport problem often exhibits oscillations at the boundary $\partial\Omega_{\mathrm{NB}}$ of the narrow band, as shown in [20].

5.1. **Weak formulation.** Now, we define the time dependent function space

$$W_{\varphi_D}(t) = \{v \in L^2(\Omega) \,:\, \vec{V}_{\Gamma_2}(\cdot,t)\cdot\nabla v \in L^2(\Omega) \wedge v|_{\partial\Omega_{\mathrm{in}}(\cdot,t)} = \varphi_D(\cdot,t)\}, \tag{5.2}$$

multiply the transport equation with an $v \in L^2(\Omega)$, and integrate over Ω so that we end up with the weak formulation: For $t \in (t_0, t_f)$ and $\zeta(\varphi_2) \in C(\Omega)$ find $\varphi_2(\cdot,t) \in W_{\varphi_D}(t)$ with $\frac{\partial\varphi_2}{\partial t} \in L^2(\Omega)$ s.t. $\varphi_2(\cdot,t_0) = \varphi_{2,0}$ and

$$\left(\frac{\partial\varphi_2}{\partial t}, v\right)_{L^2} + (\zeta(\varphi_2)\vec{V}_{\Gamma_2}\cdot\nabla\varphi_2, v)_{L^2} = 0, \quad \forall v \in L^2(\Omega),\ t \in [t_0,t_f]. \tag{5.3}$$

5.2. **Discretization in space.** For the triangulations $\{\mathcal{S}_h\}_{h>0}$ we introduce the standard Lagrangian finite element space

$$W_h^l = \{v_h \in C(\Omega_h) \,:\, v_h|_S \in \mathcal{P}_l,\ \forall S \in \mathcal{S}_h\}, \tag{5.4}$$

and define for $[t_0,t_f]$ the affine space

$$\begin{aligned} W_{h,\varphi_D}^l(t) = \{v_h \in C(\Omega_h) \,&: v_h|_S \in \mathcal{P}_l,\ \forall S \in \mathcal{S}_h,\\ &v(\boldsymbol{x}) = \varphi_D(\boldsymbol{x},t),\ \forall \boldsymbol{x} \in \partial\Omega_{\mathrm{in},h}(t)\}, \end{aligned} \tag{5.5}$$

with $l \geq 1$, to consider functions with Dirichlet boundary conditions on the discrete influx boundary $\partial\Omega_{\mathrm{in},h}(t)$. Using these function spaces, (5.3) discretized in space reads: For $t \in [t_0,t_f]$ find $\varphi_2(\cdot,t) \in W_{h,\varphi_D}^l$ with $\vec{V}_{\Gamma_2}(t) \in L^\infty(\Omega_h)$ and $\frac{\partial\varphi_{2,h}}{\partial t} \in L^2(\Omega_h)$ such that

$$\sum_{S\in\mathcal{S}_h}\left(\frac{\partial\varphi_{2,h}}{\partial t} + \zeta_h\vec{V}_{\Gamma_2}\cdot\nabla\varphi_{2,h}, v_h\right)_{L^2(S)} = 0, \quad \forall v_h \in W_h^l. \tag{5.6}$$

Thereby, the polynomial degree $l = 2$ is chosen for the finite-dimensional function space (5.5). This is due to different reasons, cf. [15] and i.a. has the advantage that the degrees of freedom coincide with the degrees of freedom of linear basis functions on a regularly refined mesh. This will be used for characterizing the interface Γ_2 discretely and by the reinitialization technique.

`Remark:` Solving hyperbolic PDEs with standard finite element methods is known to be possibly instable. This is why often additional terms acting as stabilization method [35] are introduced. In our application however, there are no high velocities or big changes of $\nabla\varphi_{2,h}$ so that we can omit such terms.

Construction of the narrow band(s). The narrow band method is based on the assumption that the given discrete level set function $\varphi_{2,h}$ is an approximate signed distance function so that the DOF values are be approximately equal to the exact distance from a vertex to the interface. Using this, we define the *inner* narrow band by

$$\mathcal{V}_{\mathrm{INB}} = \{v \in \mathcal{V}(\mathcal{S}_h) \ :\ \varphi_{2,h}(v) < \gamma_h\}, \tag{5.7}$$

with $\gamma_h = \gamma h$, $\gamma \in \mathbb{Z}^+$, and $h = \max_{S\in\mathcal{S}_h}\mathrm{diam}(S)$, and the *outer* narrow band by

$$\mathcal{V}_{\mathrm{ONB}} = \mathcal{V}_{\mathrm{INB}} \cup \left(\bigcup_{v\in\mathcal{V}_{\mathrm{INB}}}\bigcup_{S\in\mathcal{P}^1(v)}\mathcal{V}(S)\right). \tag{5.8}$$

The outer narrow band thereby corresponds to all vertices of the inner narrow band set as well as all vertices of the first neighbor patch of all simplices in the inner narrow band domain. With these set, the corresponding domains $\Omega_{\mathrm{INB}} := \{S \in \mathcal{S}_h \,:\, \mathcal{V}(S) \subset \mathcal{V}_{\mathrm{INB}}\}$ and $\Omega_{\mathrm{NB}} = \Omega_{\mathrm{ONB}} := \{S \in \mathcal{S}_h \,:\, \mathcal{V}(S) \subset \mathcal{V}_{\mathrm{ONB}}\}$ can be defined.

Based on this, we define the discrete cut-off function ζ_h as

$$\begin{aligned}\zeta_h(\varphi_{2,h}) &= \zeta_h(\varphi_{2,h}(\boldsymbol{x},t)) \\ &= \begin{cases} 1 & \text{for } |\varphi_{2,h}(\boldsymbol{x},t)| \le \beta_{I,h}, \\ \hat{\zeta}_h(\varphi_{2,h},\beta_{I,h},\beta_{O,h}) & \text{for } \beta_{I,h} < |\varphi_{2,h}(\boldsymbol{x},t)| \le \beta_{O,h}, \\ 0 & \text{for } |\varphi_{2,h}(\boldsymbol{x},t)| > \beta_{O,h}, \end{cases}\end{aligned} \tag{5.9}$$

with

$$\hat{\zeta}_h = (\varphi_{2,h}(\boldsymbol{x},t) - \beta_{O,h})^2 \, \frac{2\varphi_{2,h}(\boldsymbol{x},t) + \beta_{O,h} - 3\beta_{I,h}}{(\beta_{O,h} - \beta_{I,h})^3} \tag{5.10}$$

which slowly decreases the influence of the advection term towards the boundary of Ω_{INB}. The parameters $\beta_{I,h} = \beta_I h$ and $\beta_{O,h} = \beta_O h$ with $\beta_I < \beta_O < \gamma$ divide the inner narrow band layer into three sublayers in a form that the cutoff parameter is equal to 1 in the innermost layer, tends to zero in the middle layer and is equal to zero in the outermost layer of the inner narrow band. A viable choice for these parameters is for example $\beta_I = 2,\ \beta_O = 4,\ \gamma = 6$.

5.3. **Discretization in time.** We discretize (5.6) in time using the so-called $\theta-$scheme. Please note that since the time discretization of the level set problem may differ in comparison to the discretization described in Section 3.1, we now discretize the interval $[t_0, t_f]$ by $\tilde{N}_t + 1$ time steps $t_n = t_0 + n\tilde{\Delta}t$, $n = 0, \dots, \tilde{N}_t$ with $\tilde{\Delta}t$ denoting the time step. Let $\theta \in [0,1]$ be a parameter and $\varphi_{2,h}^n(\cdot) \approx \varphi_2(\cdot, t_n)$ be an approximation of the level set function φ_2 at time t_n, the completely discretized level set problem then reads

$$\begin{aligned}&\sum_{S\in\mathcal{S}_h} \left(\tfrac{\varphi_{2,h}^{n+1} - \varphi_{2,h}^n}{\tilde{\Delta}t} + \theta\zeta_h^{n+1}\vec{V}_{\Gamma_2}^{n+1}\cdot\nabla\varphi_{2,h}^{n+1} + (1-\theta)\zeta_h^n\vec{V}_{\Gamma_2}^{n}\cdot\nabla\varphi_{2,h}^{n}, v_h \right)_{L^2(S)} \\ &\qquad = 0, \quad \forall v_h \in W_h^2.\end{aligned} \tag{5.11}$$

Therein, we treat (5.9) explicitly with respect to time by defining $\zeta_h^{n+1} = \zeta(\varphi_{2,h}^n)$ to avoid the task of solving a non-linear equation. For doing so, the innermost narrow band layer width $\beta_I h$ has to be chosen to be sufficiently large.

5.4. **Representation of Γ_2.** While we used an arbitrary approximation $\Gamma_{2,h}$ of Γ_2 for the (formal) discretization of the thermal problem in Section 3, the XFEM representation is based on the approximating Γ_2 linearly which results in planar intersection segments. Hence, we use the representation technique of [15] which also provides a detailed investigation about the approximation quality and the discretization error for this approach:

For $t_n = t_0 + n\tilde{\Delta}t$, $n = 0, \dots, \tilde{N}_t$, let $\varphi_{2,h}^n \in W_h^2$ be the finite element approximation of the level set function $\varphi_2(\cdot, t_n)$ and $\bar{\Gamma}_{2,h}^n$ its zero level. We define the set of simplices containing $\bar{\Gamma}_{2,h}^n$ by

$$\mathcal{S}_h^{\Gamma_2}(t_n) := \left\{ S \in \mathcal{S}_h \,:\, \text{meas}_2(S \cap \bar{\Gamma}_{2,h}^n) > 0 \right\} \tag{5.12}$$

and introduce $\mathcal{S}_{h/2}^{\Gamma_2}(t_n)$ as the set consisting of all simplices that are obtained, if the elements in $\mathcal{S}_h^{\Gamma_2}$ are regularly refined. The finite element approximation $\varphi_{2,h}^n$ of φ_2^n is then linearly interpolated by $I\varphi_{2,h}^n$ using standard Lagrange interpolation on the patch of refined elements $S \in \mathcal{S}_{h/2}^{\Gamma_2}(t_n)$ and the discrete approximation of Γ_2^n is given by

$$\Gamma_{2,h}^n := \left\{ \boldsymbol{x} \in \Omega \,:\, I\varphi_{2,h}^n(\boldsymbol{x}) = 0 \right\}. \tag{5.13}$$

5.5. **Maintaining techniques.** As mentioned earlier, it is not only beneficial to have a level set function φ_h which is close to a signed distance function but mandatory for the narrow band approach. Unfortunately, the signed distance property may be lost during the evolution of the level set function in time due to various reasons, e.g. discretization errors, insufficient approximation of the curvature and topological changes. Therefore, the level set function has to be reinitialized. In our approach, we use a variant [15] of the Fast Marching Method (FMM) [39], providing a signed distance approximation $\tilde{\varphi}_h$ of φ_h. Since the FMM slightly distorts the interface $\Gamma_{2,h}$ and, consequently, is not volume-preserving, a volume correction algorithm must

be additionally applied. Both methods are described in detail in [18] and some more notes about the idea and the technical implementation can be found in [15] and [17].

5.6. **Construction of a velocity field.** The evolution of the level set function φ_2 is driven by the velocity $\vec{V}_{\Gamma_2}$. In regards to the Stefan problem, this velocity field $\vec{V}_{\Gamma_2}^n \in (W_h^1)^d$ can be computed using the Stefan condition (2.14), which discretely reads

$$[\![\lambda \nabla u_h^n]\!] \cdot \vec{n}_{2,h} = \rho L \vec{V}_{\Gamma_2}^n \cdot \vec{n}_{2,h} \quad \text{on } \Gamma_{2,h}^n, \quad n \in \{1, \dots, N_t\}. \tag{5.14}$$

In our method, we compute $\vec{V}_{\Gamma_2}$ in two steps: In the first step, equation (5.14) is used to compute the velocity at the interface by either evaluating the gradient ∇u_h^n on $\Omega_{2,h}^n$ and $\Omega_{3,h}^n$ directly or by evaluating an approximation of the gradient based on a regression scheme using several point evaluations [6]. This velocity is then extended to the whole narrow band in a second step, making this approach very similar to the Fast Marching Method. We refer again to [18] for details.

6. Computational approach and some implementation aspects

For the numerical simulation of keyhole-based welding, we split the process into three sub-problems by firstly distinguish between the problems "computing the keyhole geometry" and "solving the coupled thermal problem" and then by decoupling heat equation and level set problem. While in the presented approach the computation of the keyhole geometry is based on an analytical approach which is independent of the (remaining) sub-problems, the decoupling of the thermal problem and the level set problem result in different aspects which have to be considered within the numerical method.

6.1. **Decoupling of the thermal problem.** The thermal problem with given $\Gamma_1(t)$ for $t \in [t_0, t_f]$ consists of the sub-problems (2.15) and (2.17) which are coupled by the Stefan condition (2.16). In this article, we use the same strategy as in our previous work [18] and decouple the heat equation and the level set problem by solving both in succession: Given all data for t_n, we

(1) determine the interface's normal velocity $\vec{V}_{\Gamma_2}^{n+1} \cdot \vec{n}$ and the velocity field $\vec{V}_{\Gamma_2}^{n+1}$ using the approaches presented in Section 5.6,
(2) solve the level set problem (2.17) to obtain φ_h^{n+1} and the new interface $\Gamma_{2,h}^{n+1}$,
(3) construct new XFEM function spaces and solve the thermal problem (2.15) for u^{n+1}.

Thereby, we use the implicit Euler scheme for time discretization in both subproblems. However, due to the narrow band approach and the decoupling strategy, the time discretization of level set problem and heat equation may still differ since we may need intermediate time steps as CFL conditions arise.

6.2. **CFL conditions.** For the numerical solution of the thermal problem (2.15)-(2.17), two different types of CFL conditions have to be considered. The first CFL condition is motivated by the physical behavior of the material while the second and third CFL condition are technical constraints which are introduced by the narrow band approach.

6.2.1. *Physically motivated CFL condition.* The first CFL condition is introduced by (2.7) which includes that vapor and melt are separated by the isoline of the vaporization, just as the molten and solid material are separated by the isoline of the melting temperature. For the simulation, it follows that although keyhole wall Γ_1 and solid-liquid interface Γ_2 are considered as zero level sets of separate independent level set functions φ_1 and φ_2, the model does not allows that Γ_1 and Γ_2 intersect or touch each other, cf. Section 2.1. In fact, Γ_2 can only be defined outside the keyhole where $u < u_{\Gamma_1}$ so it is $\Gamma_2 \nsubseteq \Omega_1$.

`Remark:` While this condition can be easily met by choosing an arbitrarily small time step size, one is interested in choosing a time step size which is close the largest possible step size due to efficiency. Therefore, one can either compute the time step size for every step using the previously determined values of welding speed $\vec{V}_w$, interface velocity $\vec{V}_{\Gamma_2}$ and minimum distance between Γ_1 and Γ_2 or define a reasonable value a priori and check every step regarding a violation of the CFL condition.

6.2.2. *CFL conditions due to the narrow band approach.* A consequence of the narrow band approach is that one has to consider the following two CFL conditions:

- Since ζ decreases the transport of the level set function everywhere but in the most inner band, the velocity $\vec{V}_{\Gamma_2}$ must not exceed a value which would make the interface $\Gamma_{2,h}$ leave this region. Therefore, the CFL condition

$$\Delta t \| \| \vec{V}_{\Gamma_2}^n \|_2 \|_{L_\infty(\Omega_{\mathrm{INB}})} < \beta_{I,h}, \quad \forall n \in \{0, \dots, \tilde{N}_t\} \tag{6.1}$$

  must hold.
- For constructing $\Omega_{\mathrm{INB}}^{n+1} \subset \Omega_{\mathrm{ONB}}^n$, we need $\varphi_{2,h}$ to be close to a signed distance function on Ω_{ONB}^n. If the velocity transporting the interface is too big, we may end up considering the constant values $\pm(\gamma_h + \varepsilon)$ during the solution and reinitialization process. To avoid this, the condition

$$\Delta t \| \| \vec{V}_{\Gamma_2}^n \|_2 \|_{L_\infty(\Omega_{\mathrm{INB}})} < h, \quad \forall n \in \{0, \dots, \tilde{N}_t\}. \tag{6.2}$$

  has to be respected.

`Remark:` A typical parameter choice includes $\beta_I > 1$ so that (6.1) is automatically fulfilled, if (6.2) holds, making this the limiting condition. Please also note that even though the method's description assumes the reinitialization procedure to be applied after *every* time step, it might be better to apply reinitialization and update the narrow band after every m-th time step instead. This results in a more restrictive CFL condition given by

$$m\Delta t \| \| \vec{V}_{\Gamma_2}^n \|_2 \|_{L_\infty(\Omega_{\mathrm{INB}})} < h, \quad \forall n \in \{0, \dots, \tilde{N}_t\}. \tag{6.3}$$

6.3. **Synchronization of time steps.** As a consequence of the CFL conditions or the possible use of different time discretization schemes for the thermal problem (2.15) and the level set problem (2.17), the discrete time steps in both problems may not coincide. Since common time steps are mandatory for our decoupling strategy to work, we have to explicitly synchronize the time step sizes for the subproblems.

For this purpose, we define the time step size Δt of the thermal problem as so-called major time step size and use the values $t_n = t_0 + n\Delta t$ with $n \in \{0, \dots, N_t\}$, cf. Section 3.1, as synchronization points. The time step size Δt_φ used for the discretization of the level set problem is then adjusted by introducing (potentially) non-equidistant intermediate time steps $t_{n,i}$ so that both, the time step size $\tilde{\Delta t}$ caused by a different time discretization scheme and time step size Δt_{CFL} to fulfill the CFL conditions, are respected. The described procedure is illustrated in Figure 6.1

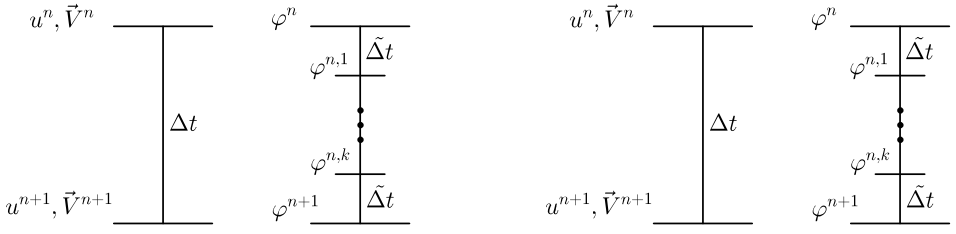

(a) Time stepping for different discretization schemes

(b) Time stepping due to CFL conditions

FIGURE 6.1. Time stepping synchronization: Intermediate time steps for the solution of the level set problem are synchronized with the time step size for the thermal problem.

Algorithm 1 Numerical approach to simulate laser-based keyhole welding using `miXFEM` and the `FEniCS` framework

Require: $\Omega,\ \Gamma_D,\ \Gamma_N,\ \Gamma_R,\ g_D,\ g_N,\ \mathcal{S}_h,\ \Delta t,\ \beta_O,\ \beta_I,\ \gamma,$ material/process parameters.
Ensure: $u_h^n,\ \Gamma_{1,h}^n,\ \varphi_{1,h}^n,\ \Gamma_{2,h}^n,\ \varphi_{2,h}^n,\ \vec{V}_{\Gamma_2}^n$ for $n = 0, \dots, N_T$.

Initialization:

Compute keyhole geometry with the model presented in Section 4.4 and Section 4.5 and obtain $\varphi_{1,h}$ and $\Gamma_{1,h}^0$ via (4.18).
Compute a temporary guess for $\hat{u}_h^0$ by solving the heat equation with $\Gamma_{1,h}^0$ as discontinuity for one small time step $\hat{\Delta}t$.
Construct $\varphi_{2,h}^0$, first defining $\varphi_{2,h}^0 = -(\hat{u}_h^0 - u_{\Gamma_2})$ so that $\Gamma_{2,h}$ corresponds to the melting temperature and then performing a reinitialization step.
Compute u_h^0 by solving the heat equation with $\Gamma_{1,h}^0$ and $\Gamma_{2,h}$ as discontinuities for one small time step $\tilde{\Delta}t$
if narrow band method is used **then**
  initialize Ω_{INB} and Ω_{ONB} with $\varphi_{2,h}$.
end if

Time stepping:

for $n = 0, \dots, N_t - 1$ **do**
  Compute the velocity field $\vec{V}_{\Gamma_2}^n$ with one of the methods described in Section 5.6.
  Check first CFL condition described in Section 6.2.1 and adapt Δt if necessary.
  Assign $t_\varphi = n\Delta t$ (current simulation time) and $\varphi_{2,h}^{t_\varphi} = \varphi_{2,h}^n$.
  while $t_\varphi < (n+1)\Delta t$ **do**
    Assign largest allowed time step to Δt_{CFL} such that CFL conditions (6.1) and (6.3) are satisfied.
    Compute time step for level set propagation $\Delta t_\varphi = \min\{\Delta t_{\text{CFL}}, (n+1)\Delta t - t_\varphi\}$.
    Propagate level set function with $\vec{V}_{\Gamma_2}^n$ to obtain an updated level set function $\varphi_{2,h}^{t_\varphi + \Delta t_\varphi}$.
    if reinitialization is necessary **then**
      Replace $\varphi_{2,h}^{t_\varphi + \Delta t_\varphi}$ by its reinitialized version.
      if narrow band method is applied **then**
        Update inner and outer narrow band regions $\Omega_{\text{INB}},\ \Omega_{\text{ONB}}$ with the reinitialized function $\varphi_{2,h}^{t_\varphi + \Delta t_\varphi}$.
      end if
    end if
    Set $t_\varphi = t_\varphi + \Delta t_\varphi$.
  end while
  Set $\varphi_h^{n+1} = \varphi_{2,h}^{t_\varphi}$.
  Compute $\varphi_{1,h}^{n+1}$ by moving $\varphi_{1,h}^n$ with $\vec{V}_{\text{L}}$.
  Update function spaces considering $\varphi_{1,h}^{n+1}$ and $\varphi_{2,h}^{n+1}$ as discontinuities, all boundaries resp. boundary conditions and solve the heat equation (3.24) to get the new temperature approximation u_h^{n+1}.
end for

6.4. **Implementation framework.** The full numerical approach for the simulation of laser-based keyhole welding including the Stefan problem in level set formulation is shown in pseudo code in Alg. 1. This procedure is implemented using `miXFEM` and a level set toolbox, both developed within our work group for the `FEniCS` framework. The resulting library allows for the automated solution of problems involving arbitrary discontinuities which may evolve and also intersect each other. The advantage of the automated approach is that the use can use a high abstraction level to define the variational formulation of the problem at hand and use a specifically developed compiler which generates the corresponding low-level C++ code.

6.4.1. *The FEniCS project.* `FEniCS` is a collaborative project of researchers who develop tools for automated scientific computing, especially in the field of finite element methods for the solution of partial differential equations [25]. It consists of a collection of core components such as

(1) the Unified Form Language `UFL` [4], which is a domain-specific language to specify finite element discretizations of differential equations using variational formulations close to the mathematical notation,
(2) the `FEniCS` Form Compiler `FFC` [23, 32], which analyzes given `UFL` code and, in combination with `Instant` and `FIAT` [22], generates `UFC` [3] code for arbitrary finite elements on simplices based on the variational forms specified in the `UFL` file,
(3) `DOLFIN` [26], the main problem solving environment and user interface whose functionality integrates the other `FEniCS` components and handles communication with external libraries or toolboxes such as `miXFEM`.

6.4.2. *miXFEM - an XFEM toolbox for FEniCS.* `FEniCS` provides a lot of useful classes, structures and other utilities for the automated solution of PDE based problems with the conventional finite element method. However, it has to be extended by new modules for considering non-standard problems. In order to solve problems with arbitrary time-dependent discontinuities, we developed an XFEM toolbox [16, 19] partly based on the `PUM` toolbox [29, 30].

For this to work, `miXFEM` adds features to the domain specific language `UFL` in order to define enriched function spaces. Additionally a new syntax for integrals on arbitrary interfaces is introduced. The `UFL` file is compiled using an extended `FeniCS` Form Compiler, which understands and interprets the new features, to generate the corresponding C++ code. Based on this code, the problems can be solved numerically using an extension of the `DOLFIN` library, implemented in C++. While some key features are presented in [19], a detailed technical description of all features is given in [16].

6.4.3. *Level set toolbox.* Another extension to `FEniCS` used to solve problem (2.15)-(2.17) is a level set toolbox, which is used to compute the evolution of the level set function resp. the discontinuity. The toolbox consists of discretized weak formulations for different time stepping schemes formulated in `UFL` and compiled with the `FFC` which are used by a C++ library. This library provides an implementation of the presented Fast Marching Method and the volume correction approach which can be used for various problems. A detailed description is given in [17]. For efficiency, all computations can be performed on a narrow band mesh.

7. Results

The presented model is used to simulate keyhole-based laser welding for the materials aluminum 3.2315, steel 1.0330 and steel 1.4301 whose material properties are given in Table 1[1]. While we firstly comment on the effect of multi-reflections on the keyhole shape, the main aspect of this section is the comparison of experimental results and the simulation findings. For this purpose, our cooperation partner the Bremer Institut für angewandte Strahltechnik (BIAS) has performed experimental studies with varying parameters for the welding speed V_{L} and laser power P_{L} for each material so that we can compare the simulation outputs wit real experimental results.

7.1. **Simulation setup.** For the simulation, we use an implicit Euler scheme for time discretization and the polynomial degree $k = 1$ for the discrete space V_h^k so that the temperature is a linear function. The time step size $\Delta t \in [5 \cdot 10^{-6}\, s,\ 5 \cdot 10^{-4}\, s]$ is computed during the run time for each step by the evaluating the CFL condition (6.2). The mesh is consists of regions with different element sizes where it is $h_{\min} = 4 \cdot 10^{-}5$ and $h_{\max} = 3 \cdot 10^{-}3$ to allow for a sufficiently efficient computation with respect to all scenarios but is of course not *fitted* to the internal boundaries $\Gamma_{1,h}$ and $\Gamma_{2,h}$ at all. A section of the simulation output during the process is exemplary shown in Figure 7.1 using the software `ParaView` [5]. In lack of better data, we assume that the initial radii of the keyhole at the front, back and side are given by the laser spot radius for all simulation runs.

[1]When no value is known, we use for the steel the corresponding value of iron and for aluminum 3.2315 the value of pure aluminum.

TABLE 1. Material properties of steel 1.4301, steel 1.0330 and aluminum 3.2315 [13, 33, 38].

symbol	**1.4301**	**1.0330**	**3.2315**	**description**
u_0	300 K	300 K	300 K	initial temperature
u_a	300 K	300 K	300 K	ambiance temperature
u_m	1673 K	1700 K	933 K	melting temperature
u_v	3000 K	3000 K	2800 K	evaporation temperature
ρ	7900 kg/m^3	7860 kg/m^3	2700 kg/m^3	density
c_p	830 J/kg K	460 J/kg K	900 J/kg K	specific heat capacity
λ_s	15 J/mK	60 J/mK	160 J/mK	thermal conductivity in solid
λ_l	35 J/mK	40 J/mK	110 J/mK	thermal conductivity in melt
L	276000 J/kg	276000 J/kg	386000 J/kg	latent heat
α_{fr}	0.38	0.36	0.20	absorption coefficient

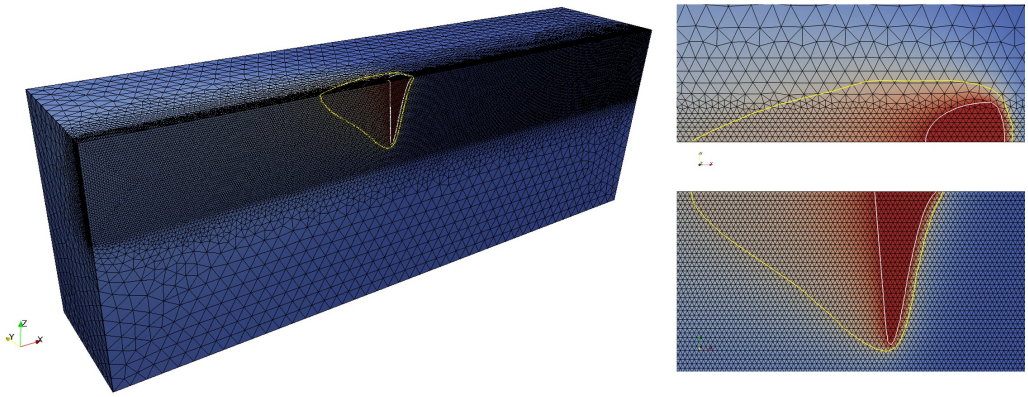

FIGURE 7.1. Visualization of simulation results for steel 1.0330 with $V_{\text{L}} = 4$ m/min and $P_{\text{L}} = 2000$ W. Keyhole is indicated by the white line, solid-liquid interface is visualized in yellow. The XFEM approach allows for considering mesh independent discontinuities.

7.2. **Effect of multi-reflection on the keyhole geometry.** As described in Section 4.5, only the portion α_{fr} of the intensity is absorbed when a ray impinge at the material while the remaining part $1 - \alpha_{\text{fr}}$ is reflected. Hence, the important characteristic in keyhole-based laser welding is the partial absorption of a multiple reflected laser ray at each wall contact. To point out the impact of this effect, Figure 7.2 shows an example of the keyhole shape without and with multi-reflections for the material steel 1.4301 with $\alpha_{\text{fr}} = 0.38$, $V_{\text{L}} = 4$ m/min, and $P_{\text{L}} = 2000$ W. In this example, it can be observed how the inclusion of multi reflections generates a keyhole keeping the same width but getting at least twice the penetration length of the keyhole into the material.

For simplicity, many publications that address welding processes neglect multi reflections. Instead, the Fresnel absorption rate is chosen significantly higher in order to compensate their impact. Using the same scenario as before, Figure 7.3 shows the keyhole shape with multi-reflections compared to a situation with $\alpha_{\text{fr}} \approx 0.6$ where no reflections are considered. This can be done, but has a high risk of choosing a wrong scaling factor. Notice in the example of Figure 7.2 that the same penetration depth was obtained, but the geometric shapes differ, specially in the lowest part of the keyhole. Furthermore, the scaling factor taken here to get the same penetration depth was around 1.58, which is not straightforward to know and might only be useful for this specific combination of material, laser configuration and process speed.

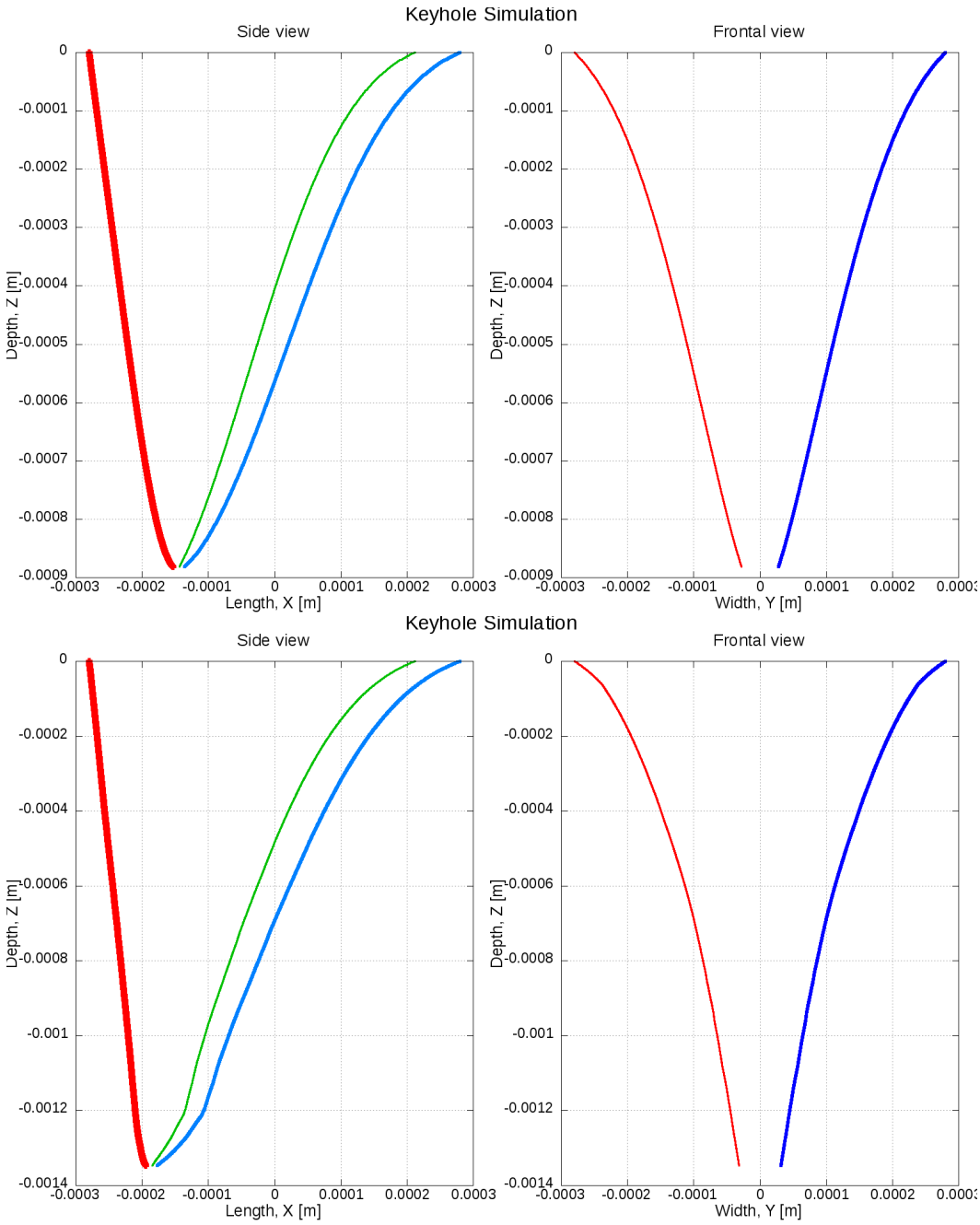

FIGURE 7.2. Keyhole geometries without (top) and with multi-reflections (bottom) for the material steel 1.4301 and the parameters $\alpha_{\mathrm{fr}} = 0.38$, $V_{\mathrm{L}} = 4$ m/min, and $P_{\mathrm{L}} = 2000$ W.

7.3. **Keyhole-based laser welding for different materials.** Now, we consider keyhole-based laser welding for the materials steel 1.4301, steel 1.0330 and aluminum 3.2315. As mentioned, the BIAS has performed several experiments for each material using different parameters for the welding speed V_{L} and laser power P_{L}. The experimental design is as visualized in the introduction. In more detail, specimens of size 100 mm $\times$ 40 mm $\times$ 6 mm are welded by a single-mode fiber laser IPG YLR-1000SM with Gaussian beam profile that is applied to the $x - y$ plane of the metal sheets. In all experiments, no shielding gas is present.

The results of the experiments and simulation runs for each material and process parameter configuration are given in the Table 2 for aluminum 3.3215, in Table 3 for steel 1.0330, and in Table 4 for steel 1.4301. In these tables, it can be seen that the simulation always underestimates

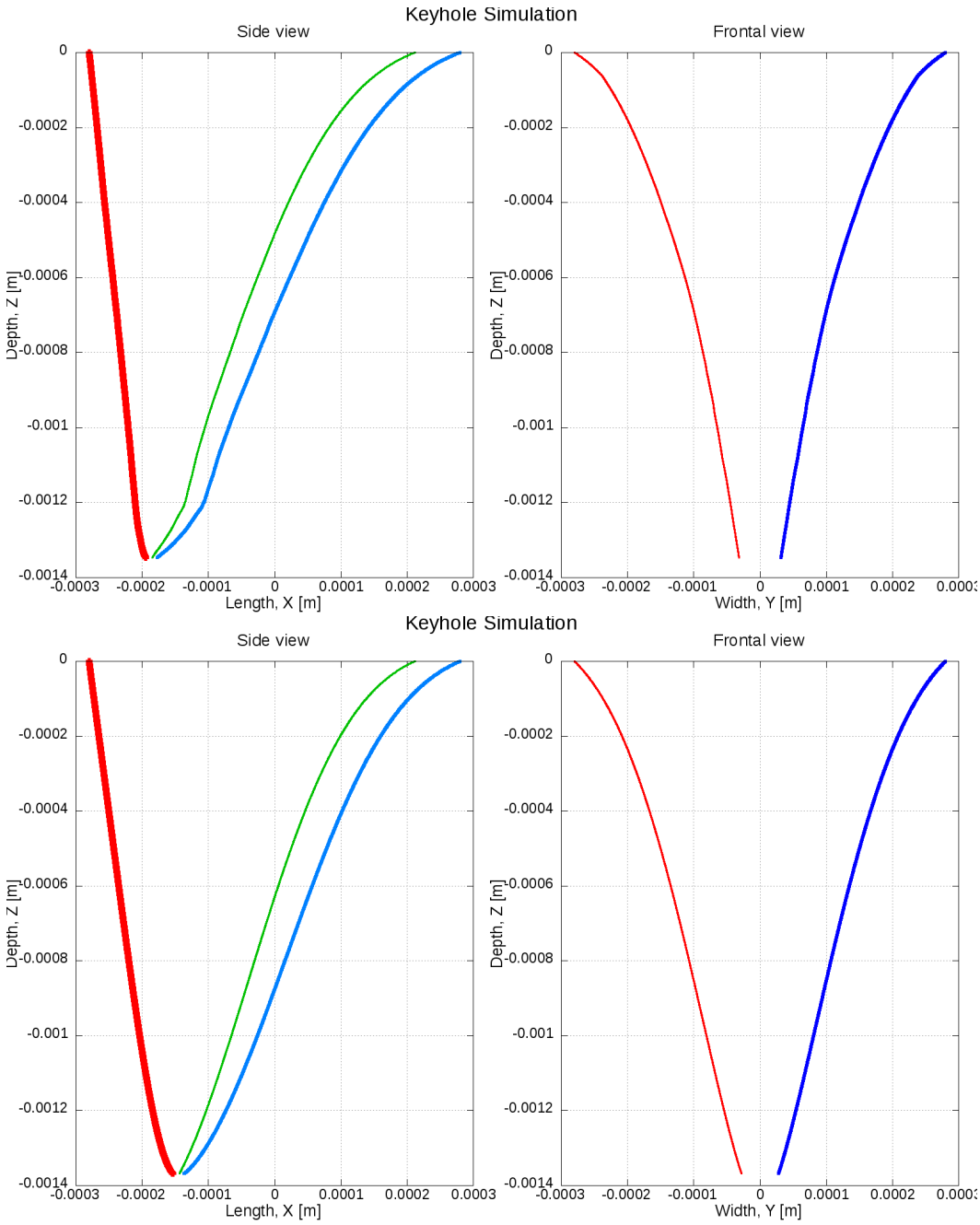

FIGURE 7.3. Keyhole geometries with multi-reflections for $\alpha_{\mathrm{fr}} = 0.38$ (top) and without multi-reflections but $\alpha_{\mathrm{fr}} \approx 0.60$ (bottom) for steel 1.4301 using the parameters $V_{\mathrm{L}} = 4$ m/min and $P_{\mathrm{L}} = 2000$ W.

the melt pool width while the measured and simulated melt pool depth coincides very well. Comparing the experimental data to the numerical results, cf. Figure 7.4 for aluminum, Figure 7.5 for steel 1.0330, and Figure 7.6 for steel 1.4301, the smaller melt pool width in all simulation runs is obviously a consequence of neglecting the melt dynamics in the model which would have a significant influence in the upper part of the melt pool due to buoyancy forces. This assumption is supported by the fact that the difference in the melt pool width decreases for increasing welding speed.

TABLE 2. Experimental data and numerical results for aluminum 3.2315.

P_L	V_L	z_exp	$w_\mathrm{exp,0.5}$	z_sim	w_sim
3000 W	5 m/min	1.31 mm	2.22 mm	1.32 mm	1.75 mm
3000 W	6 m/min	1.25 mm	1.66 mm	1.25 mm	1.67 mm

TABLE 3. Experimental data and numerical results for steel 1.0330.

P_L	V_L	z_exp	$w_\mathrm{exp,0.5}$	z_sim	w_sim
2000 W	4 m/min	1.45 mm	1.20 mm	1.48 mm	1.00 mm
2000 W	5 m/min	1.10 mm	1.11 mm	1.27 mm	0.99 mm

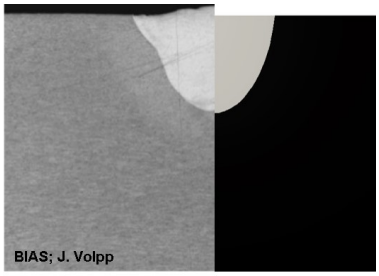

(a) aluminum 3.2315, $P_\mathrm{L} = 3000$ W, $V_\mathrm{L} = 5$ m/min.

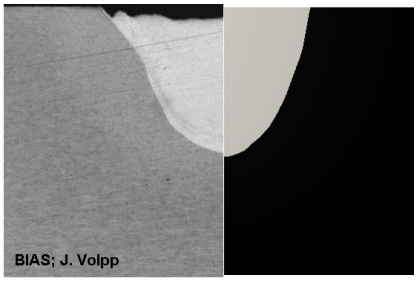

(b) aluminum 3.2315, $P_\mathrm{L} = 3000$ W, $V_\mathrm{L} = 6$ m/min.

FIGURE 7.4. Melt pool geometry: Experimental and numerical results for aluminum 3.2315.

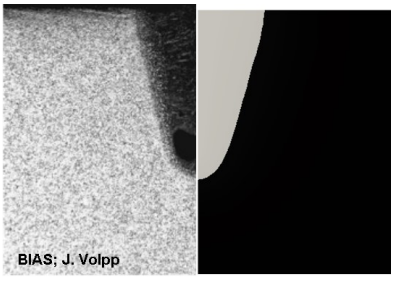

(a) steel 1.0330, $P_\mathrm{L} = 2000$ W, $V_\mathrm{L} = 4$ m/min.

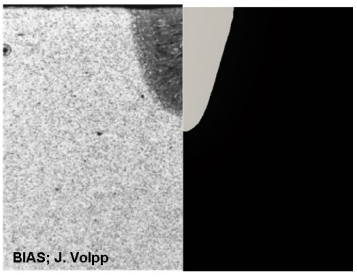

(b) steel 1.0330, $P_\mathrm{L} = 2000$ W, $V_\mathrm{L} = 5$ m/min.

FIGURE 7.5. Melt pool geometry: Experimental and numerical results for steel 1.0330.

TABLE 4. Experimental data and numerical results for steel 1.4301.

P_L	V_L	z_exp	w_exp	z_sim	w_sim
2000 W	4 m/min	1.53 mm	1.24 mm	1.45 mm	1.02 mm
2000 W	5 m/min	1.21 mm	1.13 mm	1.26 mm	1.00 mm

8. CONCLUSION

In this article, an extended finite element approach for laser-based keyhole welding modeled by heat equation with two internal boundaries has been presented. Using an analytical model based

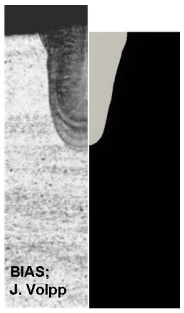

(a) steel 1.4301, $P_{\mathrm{L}} = 2000$ W, $V_{\mathrm{L}} = 4$ m/min.

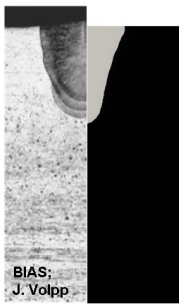

(b) steel 1.4301, $P_{\mathrm{L}} = 2000$ W, $V_{\mathrm{L}} = 5$ m/min.

FIGURE 7.6. Melt pool geometry: Experimental and numerical results for steel 1.4301.

on the energy balance at the keyhole wall, a computation scheme provided coordinates of points at the front, rear and side keyhole wall. These points have been used to construct a section-wise defined level set function whose zero level set represented the keyhole shape. The evolution of the solid-liquid interface was computed by considering the two-phase Stefan problem in level set formulation in the remaining domain outside the keyhole. Thereby, the thermal problem and the transport equation are only coupled by the Stefan condition providing the interface's velocity so that an explicit decoupling strategy could be used where level set problem and heat equation have been considered in succession. Moreover, this modeling allowed for discretizing both subproblems using different methods. The numerical computation of the level set function's evolution is a standard problem and is here performed on a narrow band for efficiency. Since the level set function tends to degenerate, not only SUPG stabilization but also reinitialization via the fast marching method has been included in the numerical approach. In regards to the thermal problem, a general concept of enriching the function space via local Heaviside enrichment was used and the interface conditions at the keyhole wall and the solid-liquid interface have been weakly imposed with Nitsche's method. The discrete problem at hand was solved using `miXFEM`, our XFEM toolbox for `FEniCS`. For validation, experimental data for keyhole-based laser welding applied to the materials steel (1.4301, 1.0330) and aluminum (3.2315) are used, where the process parameters welding speed $\vec{V}_{\mathrm{L}}$ and laser power P_{L} are varied. The numerical results show a good fit with the experimental data although a very simple keyhole model have been used which is highly sensitive to the used material parameters. More important, the numerical approach is not only very suitable for this kind of problem but also allows for an easy modeling and integration of additional effects, e.g. fluid flow in the melt, as we will show in an upcoming publication.

ACKNOWLEDGEMENT

The authors gratefully acknowledge the financial support by the DFG (German Research Foundation) for the subproject A3 within the Collaborative Research Center SFB 747 "Mikrokaltumformen - Prozesse, Charakterisierung, Optimierung". Furthermore, we thank the Bremer Institut für angewandte Strahltechnik (BIAS) for cooperation.

References

[1] Fronts propagating with curvature-dependent speed: Algorithms based on hamilton-jacobi formulations. *Journal of Computational Physics*, 79(1):12 – 49, 1988.

[2] Modelling dendritic solidification with melt convection using the extended finite element method. *Journal of Computational Physics*, 218(1):200 – 227, 2006.

[3] M. S. Alnaes, A. Logg, K.-A. Mardal, O. Skavhaug, and H. P. Langtangen. Unified framework for finite element assembly. *International Journal of Computational Science and Engineering*, 4(4):231–244, 2009.

[4] M. S. Alnaes, A. Logg, K. B. Olgaard, M. E. Rognes, and G. N. Wells. Unified form language: A domain-specific language for weak formulations of partial differential equations. *ACM Trans. Math. Softw.*, 40(2):9:1–9:37, March 2014.

[5] U. Ayachit. *The ParaView Guide: A Parallel Visualization Application*. Kitware, Inc., USA, 2015.

[6] M. Bernauer and Roland Herzog. Implementation of an X-FEM solver for the classical two-phase Stefan problem. *Journal of Scientific Computing*, 52(2):271–293, 2012.

[7] H.S. Carslaw and J.C. Jaeger. *Conduction of heat in solids*. Oxford science publications.

[8] K. W. Cheng and T.-P. Fries. Higher-order XFEM for curved strong and weak discontinuities. *International Journal for Numerical Methods in Engineering*, 82(5).

[9] J. Chessa, P. Smolinski, and T. Belytschko. The extended finite element method (xfem) for solidification problems. *International Journal for Numerical Methods in Engineering*, 53(8).

[10] K. Chongbunwatana. Simulation of vapour keyhole and weld pool dynamics during laser beam welding. *Production Engineering*, 8(4):499–511, Aug 2014.

[11] J. Dolbow and I. Harari. An efficient finite element method for embedded interface problems. *International Journal for Numerical Methods in Engineering*, 78(2).

[12] T.-P. Fries and T. Belytschko. The extended/generalized finite element method: An overview of the method and its applications. *International Journal for Numerical Methods in Engineering*, 84(3).

[13] W.F. Gale and T.C. Totemeier. *Smithells Metals Reference Book*. Elsevier Science, 2003.

[14] J. Goldak, Aditya Chakravarti, and Malcolm Bibby. A new finite element model for welding heat sources. *Metallurgical Transactions B*, 15(2):299–305, 1984.

[15] S. Gross and A. Reusken. *Numerical Methods for Two-phase Incompressible Flows*. Springer Series in Computational Mathematics.

[16] M. Jahn. *An automated hierarchical eXtended finite element approach for multiphysics problems with discontinuities*. PhD thesis, 2018.

[17] M. Jahn and T. Klock. A level set toolbox including reinitialization and mass correction algorithms for FEniCS. Technical Report 16-01, ZeTeM, Bremen, 2016.

[18] M. Jahn and T. Klock. Numerical solution of the Stefan problem in level set formulation with the eXtended finite element method in FEniCS. Technical Report 17-01, ZeTeM, Bremen, 2017.

[19] M. Jahn and A. Luttmann. Solving the Stefan problem with prescribed interface using an XFEM toolbox for FEniCS. Technical Report 16-03, ZeTeM, Bremen, 2016.

[20] M. Kang, B. Merriman, S. Osher, D. Peng, and H. Zhao. A PDE-based fast local level set method. *Journal of Computational Physics*, 155(2):410–438, 1999.

[21] A. Kaplan. A model of deep penetration laser welding based on calculation of the keyhole profile. *Journal of Physics D Applied Physics*, 27:1805–1814, September 1994.

[22] R. C. Kirby. Algorithm 839: Fiat, a new paradigm for computing finite element basis functions. *ACM Trans. Math. Softw.*, 30(4):502–516, December 2004.

[23] R. C. Kirby and A. Logg. A compiler for variational forms. *ACM Trans. Math. Softw.*, 32(3):417–444, September 2006.

[24] M. Li, H. Chaouki, J.-L. Robert, D. Ziegler, and M. Fafard. Numerical simulation of stefan problem coupled with mass transport in a binary system through xfem/level set method. *Journal of Scientific Computing*, Jun 2018.

[25] A. Logg, K.-A. Mardal, and G. N. Wells, editors. *Automated Solution of Differential Equations by the Finite Element Method*, volume 84 of *Lecture Notes in Computational Science and Engineering*. Springer, 2012.

[26] A. Logg and G. N. Wells. DOLFIN: Automated finite element computing. *ACM Trans Math Software*, 37(2):20:1–20:28, 2010.

[27] R. Merle and J. Dolbow. Solving thermal and phase change problems with the extended finite element method. *Computational Mechanics*, 28(5):339–350.

[28] J. Montalvo-Urquizo, Z. Akbay, and A. Schmidt. Adaptive finite element models applied to the laser welding problem. *Computational Materials Science*, (1):245–254.

[29] M. Nikbakht. *Automated Solution of Partial Differential Equations with Discontinuities using the Partition of Unity Method*. PhD thesis, 2012.

[30] M. Nikbakht and G.N. Wells. Automated modelling of evolving discontinuities. *Algorithms*, pages 1008–1030.

[31] J. Nitsche. Über ein variationsprinzip zur lösung von dirichlet-problemen bei verwendung von teilräumen, die keinen randbedingungen unterworfen sind. *Abhandlungen aus dem Mathematischen Seminar der Universität Hamburg*, 36(1):9–15, 2013.

[32] K. B. Olgaard and G. N. Wells. Optimizations for quadrature representations of finite element tensors through automated code generation. *ACM Trans. Math. Softw.*, 37(1):8:1–8:23, January 2010.

[33] H. R. Shanks, A. H. Klein, and G. C. Danielson. Thermal properties of armco iron. 38:2885 – 2892, 07 1967.

[34] D. Radaj. *Eigenspannung und Verzug beim Schweißen: Rechen- und Meßverfahren*. Number 143 in Schweißtechnik. Verlag für Schweißen und verwandte Verfahren DVS-Verlag, Düsseldorf, 2002.

[35] H.G. Roos, M. Stynes, and L. Tobiska. *Robust Numerical Methods for Singularly Perturbed Differential Equations: Convection-Diffusion-Reaction and Flow Problems*. Springer Series in Computational Mathematics.
[36] D. Rosenthal. The theory of moving source of heat and its application to metal treatments. *ASME Transactions*, 48:848–866, 1946.
[37] L. I. Rubinštejn. *The Stefan Problem*, volume 27 of *Translations of Mathematical Monographs*. American Mathematical Society, Rhode Island, 1971.
[38] Lamineries MATTHEY SA. Stahl 1.4301. Technical Report 2013/01, Lamineries MATTHEY SA, Lamineries MATTHEY SA, CH-2520 La Neuveville, 2013.
[39] J. A. Sethian. A fast marching level set method for monotonically advancing fronts. *Proceedings of the National Academy of Sciences*, 93(4):1591–1595, 1996.

The Center for Industrial Mathematics, University of Bremen, 28359 Bremen, Germany
E-mail address: mischa@math.uni-bremen.de

Modeling Optimization and Computing Technology SAS de CV, 64700 Monterrey, Mexico
E-mail address: jmontalvo@moctech.com.mx